

Holographic confining-deconfining gauge theories and entanglement measures with a magnetic field

Parul Jain,^{1,*} Siddhi Swarupa Jena,^{2,†} and Subhash Mahapatra^{2,‡}

¹*Asia Pacific Center for Theoretical Physics, Pohang—37673, South Korea*

²*Department of Physics and Astronomy, National Institute of Technology Rourkela, Rourkela—769008, India*



(Received 9 January 2023; accepted 26 February 2023; published 28 April 2023)

We study various holographic pure and mixed-state entanglement measures in the confined/deconfined phases of a bottom-up AdS/QCD model in the presence of a background magnetic field. We analyze the entanglement entropy, entanglement wedge cross section, mutual information, and entanglement negativity and investigate how a background magnetic field leaves its imprints on the entanglement structure of these measures. Due to the anisotropy introduced by the magnetic field, we find that the behavior of these measures depends nontrivially on the relative orientation of the strip with respect to the field. In the confining phase, the entanglement entropy and negativity undergo a phase transition at the same critical strip length, the magnitude of which increases/decreases for parallel/perpendicular orientation of the magnetic field. The entanglement wedge cross section similarly displays discontinuous behavior each time a phase transition between different entangling surfaces occurs, while further exhibiting anisotropic features with a magnetic field. We further find that the magnetic field also introduces substantial changes in the entanglement measures of the deconfined phase; however, these changes remain qualitatively similar for all orientations of the magnetic field. We further study the inequality involving the entanglement wedge and mutual information and find that the former always exceeds half of the latter everywhere in the parameter space of the confined/deconfined phases.

DOI: [10.1103/PhysRevD.107.086016](https://doi.org/10.1103/PhysRevD.107.086016)

I. INTRODUCTION

The gauge/gravity duality or holography is an elegant theoretical framework that provides an interesting connection between quantum field theory and gravity [1–3]. In its approximate form, the duality maps a classical theory of gravity in anti-de Sitter (AdS) space to a strongly coupled quantum field theory living at the boundary of the AdS space in one lower dimension. The duality has been used to understand various aspects of strongly coupled field theories using classical gravitational tools, and by now there is plenty of evidence that numerous nonperturbative and novel aspects of strongly coupled field theories can be probed using this duality. In recent years, its applications have been found in various domains of physics ranging from condensed matter to black holes. Two of the most

promising areas where the compelling ideas of the duality can be applied to obtain important physical results are quantum information and QCD. In this paper, following up on the seminal work that combined these two areas [4,5], we further examine how the concept of pure and mixed-state entanglement measures endows the QCD phase diagram in the presence of a crucial and anisotropic parameter: the magnetic field.

Quantum information science in recent years has emerged as a powerful tool to investigate diverse aspects in theoretical physics. One of the key ingredients of quantum information is entanglement, which essentially means how different parts of the system are correlated. One of the most commonly used entanglement measures is entanglement entropy. Aspects related to entanglement entropy have been used to study quantum phases [6,7], black hole entropy [8,9], quantum communication [10,11], etc. Perhaps, one of the most striking developments appeared in the context of gauge/gravity duality, where a remarkably successful conjecture for the entanglement entropy was suggested [12,13]. In this proposal, the entanglement entropy of the boundary theory is related to the area of a certain boundary homologous minimal surface. The proposal geometrizes the concept of entanglement entropy and therefore provides a unique stage in

*parul.jain@apctp.org

†519ph2015@nitrkl.ac.in

‡mahapatrasub@nitrkl.ac.in

Published by the American Physical Society under the terms of the Creative Commons Attribution 4.0 International license. Further distribution of this work must maintain attribution to the author(s) and the published article's title, journal citation, and DOI. Funded by SCOAP³.

which spacetime geometry, quantum field theories, and quantum information measures can be combined in a single framework. Indeed, in recent years this proposal has been used to probe and investigate various physical problems, such as quantum error-correcting codes and tensor networks [14,15], large- N phase transitions [16–18], quantum gravity [19,20], confinement and deconfinement transitions [4,5], quench dynamics [21–23], etc.

The entanglement entropy, however, apart from containing UV divergences, is not a good measure of entanglement for the mixed and multipartite states. For such states, various entanglement measures, such as entanglement of formation, (logarithmic) entanglement negativity, entanglement of purification, etc., have been proposed in the quantum information literature [24–29]. These quantities generally are extremely hard to compute in strongly coupled field theories and only a handful of systems are known where these can be computed explicitly. From the gauge/gravity duality point of view, a few suggestions for these measures have appeared. This includes the entanglement of purification suggestion in Refs. [30,31], where the purification was suggested to be dual to the minimal cross-section area of the entanglement wedge E_W . Similarly, there have been two separate suggestions for the entanglement negativity. In the first suggestion, the negativity is proposed to be given by the area of an extremal cosmic brane that terminates on the boundary of the entanglement wedge [32,33], whereas in the second suggestion, it is given by certain combinations of the minimal areas of codimension-two surfaces [34–43]. Interestingly, these holographic quantities, like the entanglement entropy, are again given by the areas of certain bulk surfaces; however, unlike the entanglement entropy, they do not contain UV divergences and are finite by construction.

Let us also mention that E_W has appeared in the holographic proposal of many information-theoretic quantities. This includes the above-mentioned entanglement of purification proposal [30,31], the reflected entropy proposal [44], and the odd entropy proposal [45]. It also closely appears in the entanglement negativity proposal of Refs. [32,33]. Moreover, these different proposals of E_W do not always coincide with each other, leading to uncertainty regarding its correct holographic interpretation [46]. Therefore, it appears that more caution is required when associating an information-theoretic measure with E_W . In spite of the correct interpretational issues of E_W , a great deal of progress has been made in exploring and understanding its properties in various physical situations; see Refs. [47–64] for more details. In this work, we also take this viewpoint and investigate the properties of E_W in QCD-like holographic confined/deconfined phases in the presence of a background magnetic field, to probe its orientation- and anisotropic-dependent properties, and to see whether it provides any novel signature for confinement, without dwelling on its interpretational issues.

On the other hand, QCD is a well-tested quantum field theory of strong interactions capable of describing the subatomic physics of quarks and gluons. At low temperature and chemical potential the hadrons are bound together in a confined phase, whereas at high temperature and chemical potential these hadrons are liberated and undergo a phase transition to a deconfined quark-gluon plasma phase. Probing QCD properties in the parameter space of temperature, chemical potential, etc. is a non-trivial task and is of great importance. Unfortunately, this remains challenging in a large part of the QCD parameter space. Analytical approaches are difficult because of the strong coupling, whereas numerical-based approaches of lattice QCD are inherently Euclidean in nature. Therefore, the sparse availability of nonperturbative techniques and the failure of traditional perturbative methods have limited our understanding of QCD at strong coupling. Here, the idea of holographic duality again comes in handy and provides an elegant framework within which the strongly coupled region of QCD can be probed. Indeed, one of the main and original motivations of holography was to better understand gauge theories such as QCD at strong coupling. In particular, building a dual gravity model capable of describing real QCD features reasonably well and from which testable predictions and aspects can be obtained is important, to both complement and support other takes on the same problem, coming from, e.g., Dyson-Schwinger or functional renormalization group equations, lattice QCD, effective QCD models, etc. By now, investigations using the holographic QCD framework have been done for both string-theory-inspired top-down and phenomenological bottom-up models, and many QCD-like properties have been reproduced; see Refs. [65–68] for detailed reviews.

Recently, there have been further suggestions that another parameter might play an important role in the QCD phase structure. In particular, there are suggestions that a very strong magnetic field, of the order of $eB \sim 0.3 \text{ GeV}^2$, might be generated in noncentral relativistic heavy-ion collisions and can leave important imprints on QCD properties [69–75]. Though the produced large magnetic field decays fast after the collision, it remains sufficiently high near the deconfinement temperature and is therefore expected to modify QCD properties [76,77]. Indeed, the produced magnetic field has been shown to not only play a destructive role in the chiral and deconfinement transition temperatures (also known as inverse magnetic catalysis) [78–89], but also cause suppression/enhancement of the string tension in a direction parallel/transverse to the magnetic field [74,90,91]. Similarly, it was also suggested that it can influence the charge dynamics in QCD, thereby yielding anomaly-induced novel transport phenomena such as the chiral magnetic effect [92–94]. In the context of gauge/gravity duality as well, a lot of work has been done to construct

holographic models to mimic magnetized QCD as closely as possible. For a related discussion on the interplay between the magnetic field and QCD observables in holography, see Refs. [95–127]. Exploring QCD in the extreme external conditions of high temperature and magnetic field is not only theoretically challenging, but of direct possible relevance for current particle-accelerator-driven research programs [128], as well as the study of dense neutron stars [129], early Universe physics [130], gravitational-wave physics [131], etc.; see Refs. [132,133] for reviews.

Thus, it is clear that the magnetic field appears as an influential parameter in QCD-related physics. Therefore, it is important to investigate how this magnetic field influences information-theoretic measures in QCD phases and, in particular, whether it introduces any anisotropic features in the entanglement structure of QCD phases.

Unfortunately, getting any reliable information on the entanglement measures in interacting field theories is rather difficult. This is primarily due to severe technical difficulties inherent in both analytical and numerical calculations. For these reasons, the study of entanglement measures in QCD-like theories is quite limited. With the exception of a few lattice-related works [134–137], most studies have been based on holographic proposals. Moreover, these studies were mainly restricted to entanglement entropy. In Refs. [4,5], the authors first studied the holographic entanglement entropy in the top-down confining phases and observed a phase transition from a connected to a disconnected minimal surface as the size of the subsystem varied. This phase transition was accompanied by a change in the order of the entanglement entropy, reflecting (de)confinement. Similar nonanalytic behavior of the entanglement entropy was later observed in lattice-related studies [134,135]. This idea was then tested in many other confining models, both top-down and bottom-up, and similar results were found [138–159].

The discussion of mixed-state entanglement measures in QCD-like theories is relatively new. A short discussion appeared in Ref. [53], where E_W in a limited confining model was discussed. A thorough discussion of E_W in various top-down and bottom-up confining models was later presented in Ref. [47]; see also Ref. [54]. However, the negativity calculation only appeared in Ref. [47], and that too was restricted to the confined phase.

Until now, most studies related to probing confinement/deconfinement physics using the pure and mixed-state entanglement measures have been performed in the absence of background electromagnetic fields, in particular magnetic fields. However, as mentioned before, the magnetic field does play an important role in QCD-related physics and, therefore, can influence the entanglement structure of QCD phases. Indeed, in the presence of a magnetic field, there are several possibilities to align the entangling surfaces. For instance, we can align them

parallel or perpendicular to the magnetic field. We can hence certainly expect to find anisotropic signatures in the entanglement measures. This is interesting considering that the standard order parameter, i.e., the Polyakov loop, does depend on the magnitude of the magnetic field, but is insensitive to its direction. As such, it is again clear that further probing confinement/deconfinement physics in an anisotropic setting is important, from both theoretical and phenomenological perspectives [78,81]. For the record, let us mention that the effect of a magnetic field on the entanglement entropy in the soft-wall AdS/QCD model was discussed in Ref. [138], while no such study has been performed for the entanglement wedge, negativity, and mutual information. For discussions related to the anisotropic entanglement entropy in different contexts, see Refs. [151,160,161].

In this work, we aim to fill this gap and perform a comprehensive investigation of mixed-state entanglement measures, including both E_W and negativity, in the confined and finite-temperature deconfined QCD phases, in the presence of a background magnetic field. For this purpose, we consider the dynamical bottom-up holographic QCD model of Refs. [111,112], where a closed-form analytic solution of the Einstein-Maxwell-dilaton gravity system in the presence of a background magnetic field was obtained, thereby greatly simplifying the relevant numerical calculations, and it was shown to exhibit many desirable anisotropic QCD features. We briefly highlight this holographic model and its properties in the next section. For the entanglement entropy, we consider a strip subsystem of length ℓ in a direction either parallel or perpendicular to the magnetic field. In both cases, the entanglement entropy undergoes a phase transition from a connected surface to a disconnected surface at some critical strip length ℓ_{crit} in the confined phase. Interestingly, the magnitude of this critical strip length increases/decreases for a parallel/perpendicular magnetic field. This provides an important magnetic-field-induced signature of anisotropy in the entanglement structure. With two equal-size disjoint strips, separated by a distance x , four different types of minimal area surfaces $\{S_A, S_B, S_C, S_D\}$ appear, leading to an interesting phase diagram. This two-strip phase diagram is again greatly modified in the presence of a magnetic field, while further exhibiting anisotropic features. The mutual information turns out to be nonzero only in the S_B and S_C phases and is always a monotonic function of ℓ and x . Similarly, the entanglement wedge cross section E_W is also nonzero only in the S_B and S_C phases. Interestingly, unlike the mutual information, E_W goes to zero discontinuously for large values of x and ℓ and exhibits a nonanalytic behavior while going from the S_B to S_C phase. In particular, going from the S_B to S_C phase, the entanglement wedge cross section increases at the S_B/S_C transition line. Interestingly, this increment in the area of the

entanglement wedge at the S_B/S_C transition line decreases/increases for a parallel/perpendicular magnetic field, yielding a new anisotropic feature in the entanglement structure. We further find that E_W always exceeds half of the mutual information, i.e., the holographically suggested inequality [30] is always satisfied for both parallel and perpendicular cases. Similarly, the entanglement negativity exhibits many interesting features in the confined phase. For a single-strip subsystem, the negativity turns out to be just $3/2$ times the entanglement entropy. This suggests that the entanglement negativity also undergoes an order change, from $\mathcal{O}(N^2)$ to $\mathcal{O}(N^0)$, at ℓ_{crit} , and that the magnitude of ℓ_{crit} increases/decreases with a parallel/perpendicular magnetic field. Moreover, for two strips, the negativity behaves smoothly across various phase transition lines and there is no discontinuity in its structure. However, unlike the mutual information and entanglement wedge, the negativity can be nonzero in some parts of the S_A phase. The negativity further displays anisotropic features in parallel and perpendicular directions.

The entanglement structure of the deconfined phase is slightly simpler compared to the confined phase. In particular, there is no connected/disconnected transition and the entanglement entropy is now always given by the connected surface. This implies that it is always of order $\mathcal{O}(N^2)$. Accordingly, with two strips, there are only S_A and S_B phases, and the mutual information and entanglement wedge are nonzero only in the S_B phase, whereas the entanglement negativity is nonzero in both the S_A and S_B phases. The mutual information vanishes continuously in the S_A phase, whereas the entanglement wedge vanishes discontinuously. Moreover, the parameter space of the S_B phase is found to increase for both orientations of the magnetic field, suggesting a larger phase space for the nontrivial entanglement wedge in the presence of a magnetic field. Although the magnetic field does introduce substantial changes in the entanglement measures, these changes remain qualitatively the same in both parallel and perpendicular cases, suggesting a limited anisotropic effect of the magnetic field in the deconfined phase.

Before performing explicit calculations, let us also mention that here we model the magnetic field as a constant external field to obtain insight into the entanglement structure of QCD phases. This simplistic assumption can be justified for two reasons: (i) it has been suggested that after a fast initial decrease, the generated B is almost frozen for the rest of the lifetime of the plasma, giving more credit to the assumption of a constant B field, and (ii) from a technical point of view, it allows us to have better control

over most of the calculations and is therefore quite common in holographic magnetized QCD model building.

The paper is organized as follows. We give an introduction to the bulk gravitational theory in Sec. II, and briefly talk about the various entanglement measures that we consider for our calculations in Sec. III. We study the various entanglement measures in the presence of a background magnetic field (both parallel and perpendicular orientations) in the confining phase in Sec. IV and in the deconfining phase in Sec. V. Finally, we end the paper with discussions and conclusions in Sec. VI.

II. EINSTEIN-MAXWELL-DILATON GRAVITY WITH A MAGNETIC FIELD

In this section, we describe the relevant details of the magnetized holographic QCD model presented in Ref. [111]. The corresponding five-dimensional Einstein-Maxwell-dilaton gravitational action is given by

$$S_{\text{EM}} = -\frac{1}{16\pi G_{(5)}} \int_{\mathcal{M}} d^5x \sqrt{-g} \left[R - \frac{f(\phi)}{4} F_{MN} F^{MN} - \frac{1}{2} \partial_M \phi \partial^M \phi - V(\phi) \right], \quad (1)$$

wherein R is the Ricci scalar of the five-dimensional manifold \mathcal{M} , F_{MN} is the field-strength tensor for the $U(1)$ gauge field A_M through which a constant background magnetic field will be introduced, ϕ represents the dilaton field, and $f(\phi)$ is the gauge kinetic function which denotes the coupling between the $U(1)$ and dilaton fields. The potential for the dilaton field is given by $V(\phi)$ and $G_{(5)}$ is the five-dimensional Newton's constant. Interestingly, with an *Ansätze* for the metric g_{MN} , field-strength tensor F_{MN} , and dilaton field ϕ ,

$$ds^2 = \frac{L^2 e^{2A(z)}}{z^2} \left[-g(z) dt^2 + \frac{dz^2}{g(z)} + dy_1^2 + e^{B^2 z^2} (dy_2^2 + dy_3^2) \right], \quad (2)$$

$$\phi = \phi(z), \quad F_{MN} = B dy_2 \wedge dy_3,$$

the Einstein, Maxwell, and dilaton field equations coming from the action (1) can be completely solved in closed form in terms of a single parameter a ,

$$A(z) = -az^2, \quad (3)$$

$$g(z) = 1 - \frac{e^{z^2(3a-B^2)}(3az^2 - B^2z^2 - 1) + 1}{e^{z_h^2(3a-B^2)}(3az_h^2 - B^2z_h^2 - 1) + 1}, \quad (4)$$

$$\phi(z) = \int dz \sqrt{-\frac{2}{z} (3zA''(z) - 3zA'(z)^2 + 6A'(z) + 2B^4z^3 + 2B^2z) + K_5}, \quad (5)$$

$$f(z) = g(z)e^{2A(z)+2B^2z^2} \left(-\frac{6A'(z)}{z} - 4B^2 + \frac{4}{z^2} \right) - \frac{2e^{2A(z)+2B^2z^2}g'(z)}{z}, \quad (6)$$

$$V(z) = g'(z)(-3z^2A'(z) - B^2z^3 + 3z)e^{-2A(z)} - g(z)(12 + 9B^2z^3A'(z))e^{-2A(z)} + g(z)(-9z^2A'(z)^2 - 3z^2A''(z) + 18zA'(z) - 2B^4z^4 + 8B^2z^2)e^{-2A(z)}, \quad (7)$$

wherein the AdS radius L has been set to one and z is the usual holographic radial coordinate. The above solution is obtained by using the boundary condition $g(z = z_h) = 0$, corresponding to a black hole with a horizon at $z = z_h$. The magnetized black hole solution has the temperature and entropy

$$T = \frac{z_h^3 e^{-3A(z_h) - B^2 z_h^2}}{4\pi \int_0^{z_h} d\xi \xi^3 e^{-B^2 \xi^2 - 3A(\xi)}},$$

$$S_{\text{BH}} = \frac{V_3 e^{3A(z_h) + B^2 z_h^2}}{4G_{(5)} z_h^3}, \quad (8)$$

where V_3 is the volume of the three-dimensional spatial plane.

There also exists another solution to the field equations, corresponding to the thermal-AdS solution (without a horizon). This no-black-hole solution corresponds to $g(z) = 1$ and can be obtained by taking the limit $z_h \rightarrow \infty$ in the above equations. The coordinate z therefore runs from $z = 0$ (asymptotic boundary) to $z = z_h$ (for the black hole) or to $z = \infty$ (for thermal-AdS). Importantly, both the thermal-AdS and black hole solutions asymptote to AdS at the boundary $z = 0$, but can have a nontrivial structure in the bulk. The constant K_5 appearing in Eq. (5) is fixed by demanding that $\phi|_{z=0} \rightarrow 0$ to get an asymptotically AdS spacetime. Note that in these solutions a constant background magnetic field B is chosen in the y_1 direction, which breaks the $SO(3)$ invariance of the boundary spatial coordinates $\{y_1, y_2, y_3\}$.

Apart from its analytic simplicity, this holographic model also exhibits many desirable anisotropic QCD properties. A few salient features of this model are the following:

- (1) A Hawking/Page-type phase transition appears between the thermal-AdS and black hole solutions. In particular, the black hole phase is favored at high temperatures, whereas the thermal-AdS phase is favored at low temperatures. Accordingly, there is a phase transition between these two solutions. However, since B explicitly appears in the temperature expression, now the transition temperature is a B -dependent quantity. The behavior of the transition

temperature as a function of B for various values of a is shown in Fig. 1.

- (2) These thermal-AdS and black hole phases were further shown to be dual to confined and deconfined phases, respectively, in the dual boundary theory. Since the transition temperature decreases with B , this provided a holographic model for inverse magnetic catalysis in the deconfinement sector [111].
- (3) The parameter a is the only free parameter in this model, and Eqs. (3)–(7) form a self-consistent solution of the magnetized Einstein-Maxwell-dilaton gravity for any choice of a . Nonetheless, in the context of AdS/QCD model building, it is appropriate to fix its value by taking inputs from the dual boundary QCD theory. For instance, by demanding the confined/deconfined (or the dual Hawking/Page) phase transition temperature in the pure glue sector to be around 270 MeV, as is reported in lattice QCD [162], one fixes the value of the parameter a to be 0.15 GeV² [163]. This also fixes the largest attainable magnitude of B , by requiring the real-valuedness of the dilaton field, to be around $B \simeq 0.6$ GeV. However, it is important to note that the inverse magnetic behavior is a general result of this model that remains true for other values of a as well, as is shown in Fig. 1.
- (4) Interestingly, the string tension was further found to decrease/increase with magnetic field in longitudinal/transverse directions. These results are in good agreement with state-of-the-art lattice findings [90,91].
- (5) Similarly, the chiral critical temperature again goes down with the magnetic field, indicating inverse magnetic catalysis behavior in the chiral sector. In particular, the chiral condensate magnitude increases with B in the confined phase, whereas it exhibits

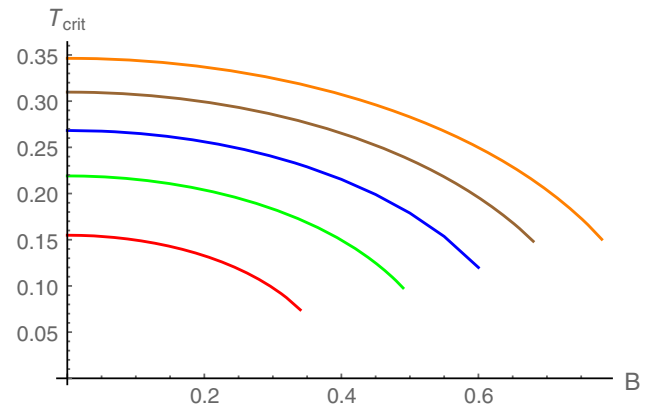


FIG. 1. Deconfinement transition temperature in terms of magnetic field for various values of a . Red, green, blue, brown, and orange curves correspond to $a = 0.05, 0.10, 0.15, 0.20,$ and 0.25 , respectively, in units of GeV.

nonmonotonic thermal features for all B in the deconfined phase. These chiral results also agree qualitatively well with lattice QCD findings, where similar features have been observed in the chiral sector.

- (6) The boundary vector-meson mass spectrum also exhibits linear Regge behavior.
- (7) As far as the stability of the model is concerned, the mass of the dilaton field ϕ satisfies the Breitenlohner-Freedman bound for stability in AdS space [164], and the dilaton potential V is bounded from above by its UV boundary value, thereby satisfying the Gubser stability criterion for a well-defined boundary theory [165]. Similarly, the null energy condition of the matter field is always satisfied and constructed geometries—both black hole and thermal-AdS spacetimes— asymptote to AdS at the boundary $z \rightarrow 0$.

We therefore see that the dual boundary theory of the model (1) indeed exhibits many desirable anisotropic QCD features with a magnetic field. Therefore, it is reasonable to use this model to find the anisotropic imprints of a magnetic field on the entanglement structure of QCD phases by studying various entanglement measures.

III. ENTANGLEMENT MEASURES

In this section, we briefly talk about various entanglement measures that have gravity duals. To probe the entanglement structure of confined/deconfined QCD phases and make the discussion complete and as general as possible, we concentrate on both pure and mixed-state measures. This includes the (i) entanglement entropy, (ii) mutual information, (iii) entanglement wedge cross section, and (iv) entanglement negativity.

A. Holographic entanglement entropy

We begin with the discussion of entanglement entropy. It is a good measure of entanglement for the pure states and in the usual quantum systems it is given by

$$S(A) = -\text{Tr}_{\rho_A} \ln \rho_A, \quad (9)$$

where ρ_A is the reduced density matrix of subsystem A , obtained by tracing out the degrees of freedom of the rest of the system. In quantum field theories, one can use the replica trick to calculate the entanglement entropy [166]. Holographically, the entanglement entropy can be computed using the Ryu-Takayanagi prescription [12,13],

$$S(A) = \frac{\mathcal{A}(\Gamma_A^{\min})}{4G_{(d+1)}}, \quad (10)$$

wherein $G_{(d+1)}$ denotes the $(d+1)$ -dimensional Newton's constant and $\mathcal{A}(\Gamma_A^{\min})$ represents the area of the

$(d-1)$ -dimensional minimal surface Γ with the condition that the boundary ∂A of the subsystem A is homologous to $\partial\Gamma$. The above equation can also be written in the following way:

$$S(A) = \frac{1}{4G_{(d+1)}} \int_{\Gamma} d^{d-1}\sigma \sqrt{\mathcal{G}_{\text{ind}}^{d-1}}, \quad (11)$$

wherein the induced metric on the surface Γ is given by $\mathcal{G}_{\text{ind}}^{d-1}$, which further needs to be minimized according to the prescription of Refs. [4,5,12,13]. For the record, we have $d = 4$ in our cases of interest.

Notice that, with a background magnetic field, we have choices to align the subsystem (or the entangling surface) with respect to the magnetic field. In particular, we can now have two interesting scenarios: (i) align the entangling surface parallel to the magnetic field, and (ii) align it perpendicular to the magnetic field. The relative orientation of the entangling surface can leave anisotropic imprints of the magnetic field on various entanglement measures. Indeed, as we will see shortly, since most of the holographic entanglement measures depend nontrivially on the bulk spacetime metric, which in turn depends nontrivially on the magnetic field, it is therefore reasonable to expect that the magnetic field might generate anisotropic features in the entanglement measures.

B. Holographic mutual information

We next move on to discuss the mutual information, which serves as a measure of entanglement for disjoint intervals. For two subsystems (A_1 and A_2), it reflects the amount of shared information between A_1 and A_2 , and in the case of two disjoint intervals on the boundary it is given as [167,168]

$$I(A_1, A_2) = S(A_1) + S(A_2) - S(A_1 \cup A_2), \quad (12)$$

wherein $S(A_1)$, $S(A_2)$, and $S(A_1 \cup A_2)$ represent the entanglement entropies pertaining to A_1 , A_2 , and $A_1 \cup A_2$, respectively. From the above equation (12), we can see that the mutual information vanishes in the case of uncorrelated systems, whereas it is nonzero for correlated systems. Moreover, the subadditivity property of the entanglement entropy further implies that the mutual information is non-negative, which in turn signifies the fact that $I(A_1, A_2)$ serves as an upper bound on the correlation between A_1 and A_2 . In the holographic context, the mutual information of the boundary system can be evaluated by computing the entanglement entropies $\{S(A_1), S(A_2), S(A_1 \cup A_2)\}$ individually from the Ryu-Takayanagi prescription. Interestingly, unlike the entanglement entropy, the holographic mutual information does not contain any UV divergences and is UV finite in nature. Therefore, it provides a cutoff or regularization-independent information. For further information related to

mutual information, see Refs. [169–175]. For more on mutual information and two disjoint interval entanglement phase structure in top-down and bottom-up QCD models, see Refs. [140,142].

C. Entanglement wedge cross section

It is well known that entanglement entropy serves as a good measure of entanglement in the case of pure states, but not so in the case of mixed states. Since entanglement entropy is known to exhibit interesting features in QCD phases, it is compelling to ask how the mixed-state measures behave in these phases. When dealing with mixed states, it turns out that the minimal area of the entanglement wedge cross section can be considered an appropriate measure holographically.¹

In order to calculate the entanglement wedge cross section holographically, we follow the method suggested in Refs. [30,31]. On the d -dimensional boundary, we consider two nonoverlapping subsystems A and B . The minimal surfaces in the $(d+1)$ -dimensional bulk corresponding to A , B , and $AB = A \cup B$ are given as Γ_A^{\min} , Γ_B^{\min} , and Γ_{AB}^{\min} , respectively. The entanglement wedge M_{AB} , which is $d+1$ -dimensional (d -dimensional, if the static case is considered), is then defined as a region in the bulk which shares its boundary with A , B , and Γ_{AB}^{\min} , implying

$$\partial M_{AB} = A \cup B \cup \Gamma_{AB}^{\min}. \quad (13)$$

It is important to see that if the size of subsystems A and B is very small or if they are too far apart, then the wedge M_{AB} will be of disconnected nature. We can further divide Γ_{AB}^{\min} as

$$\Gamma_{AB}^{\min} = \Gamma_{AB}^{(A)} \cup \Gamma_{AB}^{(B)}, \quad (14)$$

and define

$$\begin{aligned} \tilde{\Gamma}_A &= A \cup \Gamma_{AB}^{(A)}, \\ \tilde{\Gamma}_B &= B \cup \Gamma_{AB}^{(B)}. \end{aligned} \quad (15)$$

From Eqs. (14) and (15), we get the following condition for the wedge boundary ∂M_{AB} :

$$\partial M_{AB} = \tilde{\Gamma}_A \cup \tilde{\Gamma}_B. \quad (16)$$

Σ_{AB}^{\min} is then defined as a minimum surface whose boundary conditions are

¹For more information on the entanglement wedge cross section and its properties and applications in various contexts, see Refs. [47–64].

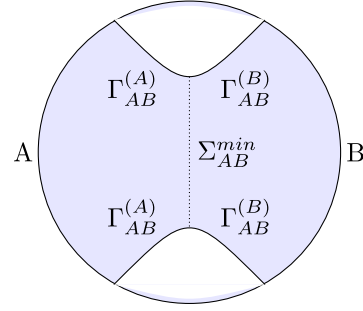


FIG. 2. The region in blue is the entanglement wedge M_{AB} corresponding to a pure state. For a thermal state, there would additionally be a black hole in M_{AB} . The dotted surface is Σ_{AB} , which divides M_{AB} into two parts.

$$\begin{aligned} (i) \quad \partial \Sigma_{AB}^{\min} &= \partial \tilde{\Gamma}_A = \partial \tilde{\Gamma}_B, \\ (ii) \quad \Sigma_{AB}^{\min} &\text{ is homologous to } \tilde{\Gamma}_A \text{ inside } M_{AB}. \end{aligned} \quad (17)$$

Using the area of Σ_{AB}^{\min} , which is denoted by $\mathcal{A}(\Sigma_{AB}^{\min})$, one can now define the entanglement wedge cross section as

$$E_W(\rho_{AB}) = \min_{\Gamma_{AB}^{(A)} \subset \Gamma_{AB}^{\min}} \left[\frac{\mathcal{A}(\Sigma_{AB}^{\min})}{4G_{(d+1)}} \right]. \quad (18)$$

To put it in words, $E_W(\rho_{AB})$ is given by the minimal area of the division of the entanglement wedge M_{AB} which connects subsystems A and B . A pictorial representation of the entanglement wedge in the connected space, i.e., in the thermal-AdS spacetime, is shown in Fig. 2.

Let us stress here once again that in recent years several entanglement measures have been suggested to be holographically dual to the entanglement wedge cross section. This includes the entanglement of purification [30,31], reflected entropy [44], and odd entropy [45]. Unfortunately, these different interpretations do not exactly coincide with each other, leading to uncertainty regarding its correct holographic interpretation. In this work, we do not dwell on the boundary interpretation issues of the entanglement wedge cross section and mainly concentrate on its properties in the confined/deconfined phases of QCD in the presence of a background magnetic field. Indeed, as we will shortly see, the entanglement wedge cross section does provide valuable information as far as the entanglement structure in the confined phase is concerned.

D. Holographic entanglement negativity

Apart from the entanglement wedge cross section, another quantity that can be taken as a suitable measure of mixed-state entanglement is entanglement negativity. In usual quantum systems this is defined as [24,25]

$$\mathcal{N} = \frac{\|\rho^{T_2}\| - 1}{2}, \quad (19)$$

where ρ^{T_2} denotes the partial transpose of the reduced density matrix and $\|\rho^{T_2}\|$ denotes its trace norm. One can further define its close cousin, the logarithmic negativity, as

$$\mathcal{E} = \ln \|\rho^{T_2}\| = \ln \text{Tr}|\rho^{T_2}|. \quad (20)$$

The logarithmic entanglement negativity serves as an upper bound to the amount of distillable entanglement and has been previously calculated in many-body systems and field theories [176–188]. In gauge/gravity duality, two seemingly different (yet equivalent) holographic proposals for the entanglement negativity are available. This includes the proposal of Refs. [32,33], in which the logarithmic negativity is given by the area of an extremal cosmic brane that terminates on the boundary of the entanglement wedge, and the proposal of Refs. [34–43], in which the logarithmic negativity is given by certain combinations of the areas of codimension-two minimal bulk surfaces. Both proposals have seemingly different mathematical definitions; however, they both reproduce independent known results for the negativity in conformal field theories and have been tested in diverse physical situations. In this work, we mainly deal with the latter proposal for two reasons: (i) the former proposal is practically similar to the computation of the entanglement wedge (which we will compute anyway), and (ii) it is computationally slightly easier to compute the negativity from the latter proposal, as opposed to the former proposal, which requires nontrivial and cumbersome cosmic brane backreaction calculation. Therefore, it might not only be complementary but also more informative if the latter proposal is adopted for the entanglement negativity calculation. Indeed, as we will see shortly, the latter proposal also provides an interesting and model-independent result for the negativity in all holographic confining/deconfining theories, which can be tested in independent lattice calculations, hence providing an intriguing platform for a nontrivial verification of the proposal.

In order to calculate the holographic logarithmic negativity in the case of a single interval, we follow Refs. [34,35] and consider a d -dimensional boundary system composed of A and its complement A^c . We now consider two additional finite intervals B_1 and B_2 adjacent

to A , implying $B = B_1 \cup B_2$; see the left part of Fig. 3. In terms of the entanglement entropy (10), the holographic logarithmic negativity is then written as

$$\mathcal{E} = \lim_{B \rightarrow A^c} \frac{3}{4} [2S(A) + S(B_1) + S(B_2) - S(A \cup B_1) - S(A \cup B_2)]. \quad (21)$$

It is important to note that in Eq. (21) both B_1 and B_2 have to be taken to infinity so that $B = B_1 \cup B_2 = A^c$.

In the case of two disjoint intervals A_1 (of length ℓ_1) and A_2 (of length ℓ_2) separated by a distance x (see the right panel of Fig. 3), the holographic logarithmic negativity is similarly written as

$$\mathcal{E} = \frac{3}{4} [S(A_1 \cup A_x) + S(A_x \cup A_2) - S(A_1 \cup A_2 \cup A_x) - S(A_x)]. \quad (22)$$

IV. CONFINING PHASE

In this section, we calculate the previously mentioned four entanglement measures in the confining phase, which is dual to the thermal AdS background, in the presence of a background magnetic field B . To compute these measures, we confine ourselves to the simplest situation where the entangling surface is a strip of length ℓ . However, this entangling strip can be placed parallel or perpendicular to the magnetic field, giving us orientation dependence of these measures.

A. Holographic entanglement entropy

1. Strip in the parallel direction

We begin by looking at the holographic entanglement entropy for a single interval and consider the boundary subsystem with the domain $\{-\ell^{\parallel}/2 \leq y_1 \leq \ell^{\parallel}/2, 0 \leq y_2 \leq \ell_{y_2}, 0 \leq y_3 \leq \ell_{y_3}\}$. Here, the strip is placed parallel to the magnetic field in the y_1 direction. In the thermal AdS background, it turns out that there are two surfaces—connected and disconnected—that minimize the entanglement entropy expression in Eq. (10). The expression of the entanglement entropy for the connected surface is found to be

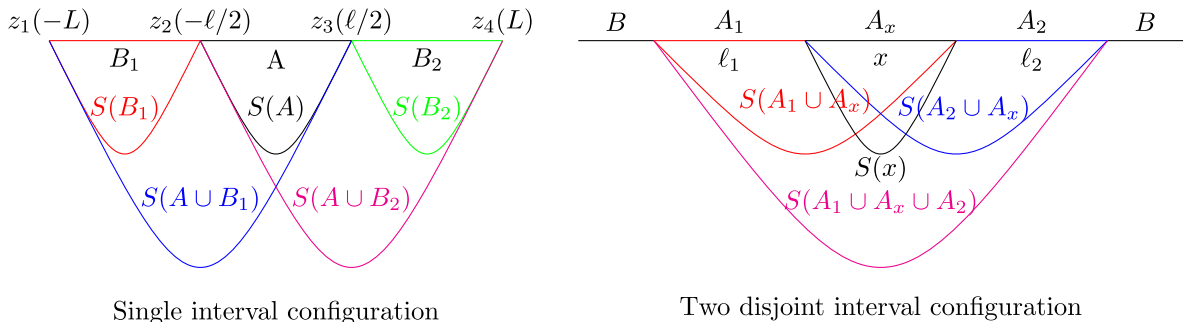


FIG. 3. The various bulk minimal surfaces that contribute to the holographic logarithmic negativity.

$$S_{\text{con}}^{\parallel} = \frac{\ell_{y_2} \ell_{y_3} L^3}{2G_{(5)}} \int_0^{z_*^{\parallel}} dz \left(\frac{z^{\parallel}}{z} \right)^3 \frac{e^{3A(z)-3A(z_*^{\parallel})} e^{B^2 z^2 - B^2 (z_*^{\parallel})^2}}{\sqrt{g(z) \left[(z_*^{\parallel})^6 e^{-2B^2 (z_*^{\parallel})^2} e^{-6A(z_*^{\parallel})} - z^6 e^{-2B^2 z^2} e^{-6A(z)} \right]}}, \quad (23)$$

where z_*^{\parallel} is the turning point of the connected surface in the bulk and is defined by $z'(y_1)|_{z=z_*^{\parallel}} = 0$. The strip length ℓ^{\parallel} in terms of z_*^{\parallel} is given by

$$\ell^{\parallel} = 2 \int_0^{z_*^{\parallel}} dz \frac{z^3 e^{-3A(z)} e^{-B^2 z^2}}{\sqrt{g(z) \left[(z_*^{\parallel})^6 e^{-2B^2 (z_*^{\parallel})^2} e^{-6A(z_*^{\parallel})} - z^6 e^{-2B^2 z^2} e^{-6A(z)} \right]}}. \quad (24)$$

The entanglement entropy expression of the disconnected surface is similarly found to be

$$S_{\text{discon}}^{\parallel} = \frac{\ell_{y_2} \ell_{y_3} L^3}{2G_{(5)}} \left[\int_0^{\infty} dz \frac{e^{3A(z)} e^{B^2 z^2}}{z^3 \sqrt{g(z)}} \right]. \quad (25)$$

Note that $S_{\text{discon}}^{\parallel}$, unlike $S_{\text{con}}^{\parallel}$, does not depend on the strip length ℓ^{\parallel} . This is an important feature that will greatly influence the properties of the entanglement measures in the confined phase. Also, note that both $S_{\text{con}}^{\parallel}$ and $S_{\text{discon}}^{\parallel}$ are UV-sensitive quantities and contain divergences. Here we adopt the minimal regularization procedure, as is generally done in the holographic literature, where these divergences are simply subtracted from the final results.

Unfortunately, it is difficult to solve the above equations analytically. However, they are straightforward to solve numerically. The numerical result for the variation of the strip length ℓ^{\parallel} with respect to the connected surface turning point z_*^{\parallel} for various values of B is shown in Fig. 4. We see that for any given value of B , there is a maximum length $\ell_{\text{max}}^{\parallel}$ above which no connected surface exists and only the disconnected surface exists. This $\ell_{\text{max}}^{\parallel}$ is a B -dependent quantity, whose magnitude not only increases but also

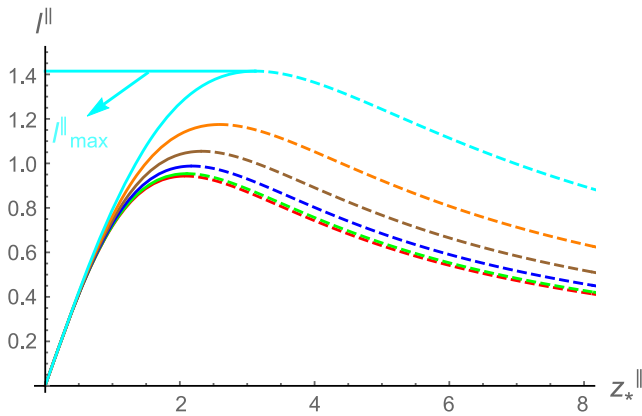


FIG. 4. ℓ^{\parallel} as a function of z_*^{\parallel} for different values of B . The red, green, blue, brown, orange, and cyan curves correspond to $B = 0, 0.1, 0.2, 0.3, 0.4,$ and 0.5 , respectively, in units of GeV.

appears at a larger z_*^{\parallel} value as B increases. This indicates that the connected entangling surface propagates deeper into the bulk for larger B values. We also see that below $\ell_{\text{max}}^{\parallel}$ there are two solutions that can minimize the connected surface area. The actual minima correspond to a solution that appears for small z_*^{\parallel} (represented by solid lines), whereas the large- z_*^{\parallel} solution corresponds to the saddle point (represented by dashed lines).

The difference between the connected and disconnected entropies $\Delta S^{\parallel} = S_{\text{con}}^{\parallel} - S_{\text{discon}}^{\parallel}$ is shown in Fig. 5 for various values of the background magnetic field.² Again, the solution for small z_*^{\parallel} is represented by solid lines, whereas the solution for large z_*^{\parallel} is represented by dashed lines. It is interesting to see that ΔS^{\parallel} goes from negative to positive values as ℓ^{\parallel} increases, suggesting that for small values of ℓ^{\parallel} $S_{\text{con}}^{\parallel}$ minimizes the entanglement entropy, whereas for large values of ℓ^{\parallel} it is $S_{\text{discon}}^{\parallel}$ that minimizes the entanglement entropy. This indicates a phase transition from connected to disconnected entropy as ℓ^{\parallel} increases. This phase transition occurs at $\ell_{\text{crit}}^{\parallel}$, which is defined by the length at which ΔS^{\parallel} becomes zero.

We further find that $\ell_{\text{crit}}^{\parallel}$ depends nontrivially on the magnetic field. In particular, its magnitude increases with B in the parallel direction. The overall behavior of the dependence of $\ell_{\text{crit}}^{\parallel}$ on B is shown in Fig. 6.

This type of phase transition between connected and disconnected entanglement entropies was first observed in top-down models in Ref. [4] and was suggested as a probe for confinement.³ In particular, such a geometric phase transition appears only in the confined phase, whereas no

²The prefactor $\ell_{y_2} \ell_{y_3} L^3 / 2G_{(5)}$, appearing in Eqs. (23) and (25), is set to one in numerical calculations.

³In Ref. [156], it was recently suggested that such connected and disconnected entanglement entropy phase transitions might be related to the mass gap rather than linear confinement.

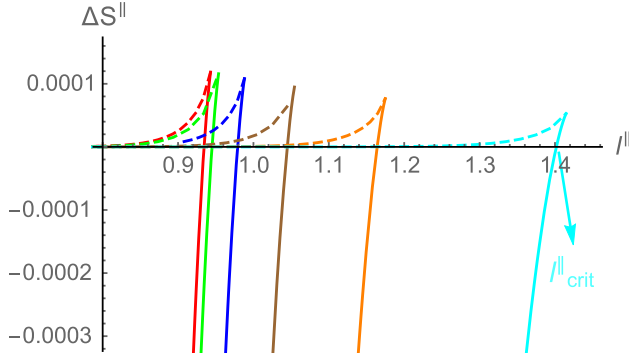


FIG. 5. $\Delta S^{\parallel} = S_{\text{con}}^{\parallel} - S_{\text{discon}}^{\parallel}$ as a function of ℓ^{\parallel} for different values of B . The red, green, blue, brown, orange, and cyan curves correspond to $B = 0, 0.1, 0.2, 0.3, 0.4,$ and 0.5 , respectively, in units of GeV.

such phase transition is observed in the finite-temperature deconfined phase. Recalling the fact that for large $\ell^{\parallel} (> \ell_{\text{crit}}^{\parallel})$ the disconnected solution becomes independent of ℓ^{\parallel} , this phase transition can be seen as follows:

$$\begin{aligned} \frac{\partial S^{\parallel}}{\partial \ell^{\parallel}} &\propto \frac{1}{G_{(5)}} = \mathcal{O}(N^2) \quad \text{for} \quad \ell^{\parallel} < \ell_{\text{crit}}^{\parallel} \\ &\propto \frac{1}{G_{(5)}^0} = \mathcal{O}(N^0) \quad \text{for} \quad \ell^{\parallel} > \ell_{\text{crit}}^{\parallel}, \end{aligned} \quad (26)$$

where N denotes the number of colors in the dual boundary theory. This implies nonanalytic behavior at $\ell_{\text{crit}}^{\parallel}$, where the number of degrees of freedom changes from $\mathcal{O}(N^2)$ to $\mathcal{O}(N^0)$, in the entanglement entropy structure of the confined phase. This type of phase transition has been observed in other holographic confining theories as well. Here we have reconfirmed this already established result, but now in a consistent bottom-up holographic QCD model in the presence of a background magnetic field. Interestingly, a similar type of nonanalyticity in the entanglement entropy has also been observed in $SU(2)$ and $SU(3)$ gauge theories using lattice simulations [134,135]. Therefore, it seems that nonanalyticity is a

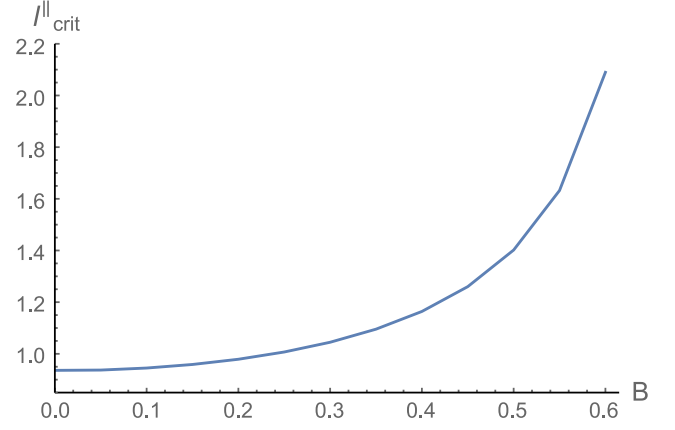


FIG. 6. $\ell_{\text{crit}}^{\parallel}$ as a function of B , in units of GeV.

generic feature of the entanglement entropy in confining theories irrespective of whether it has a gravity dual or not. To further appreciate these results, note that our holographic estimate for the length scale at which nonanalyticity appears ($\ell_{\text{crit}}^{\parallel} \simeq 0.2$ fm) is in the same ballpark as that estimated by lattice simulations ($\ell_{\text{crit}}^{\parallel} \simeq 0.5$ fm). This lends further support to the notion that certain modeling of holographic theories can yield compelling predictions for real QCD-like theories. Moreover, the result that the magnitude of $\ell_{\text{crit}}^{\parallel}$ increases with the increase of the magnetic field in the parallel direction is an important prediction of our model and could be verified in independent lattice settings (as we would not have to worry about various numerical issues, like the famous sign problem, with a finite magnetic field in lattice calculations).

2. Strip in the perpendicular direction

We now analyze the entanglement entropy in the perpendicular case. In this case, the strip subsystem, with the domain $\{0 \leq y_1 \leq \ell_{y_1}, -\ell^{\perp}/2 \leq y_2 \leq \ell^{\perp}/2, 0 \leq y_3 \leq \ell_{y_3}\}$, is aligned perpendicular to the magnetic field. There are again connected and disconnected bulk surfaces that minimize the entanglement entropy expression. The expression of the connected surface now reduces to

$$S_{\text{con}}^{\perp} = \frac{\ell_{y_1} \ell_{y_3} L^3}{2G_{(5)}} \int_0^{z_*^{\perp}} dz \left(\frac{z_*^{\perp}}{z} \right)^3 \frac{e^{3A(z) - 3A(z_*^{\perp})} e^{B^2 z^2 - B^2 (z_*^{\perp})^2} e^{-B^2 z^2/2}}{\sqrt{g(z) \left[(z_*^{\perp})^6 e^{-2B^2 (z_*^{\perp})^2} e^{-6A(z_*^{\perp})} - z^6 e^{-2B^2 z^2} e^{-6A(z)} \right]}}. \quad (27)$$

Similarly, the strip length ℓ^{\perp} in terms of the turning point z_*^{\perp} is

$$\ell^{\perp} = 2 \int_0^{z_*^{\perp}} dz \frac{z^3 e^{-3A(z)} e^{-3B^2 z^2/2}}{\sqrt{g(z) \left[(z_*^{\perp})^6 e^{-2B^2 (z_*^{\perp})^2} e^{-6A(z_*^{\perp})} - z^6 e^{-2B^2 z^2} e^{-6A(z)} \right]}}. \quad (28)$$

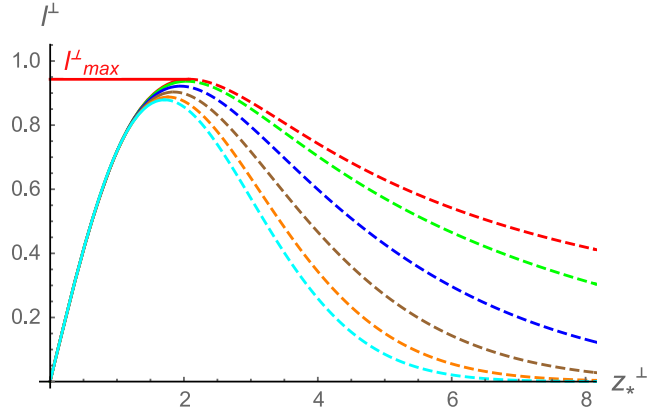


FIG. 7. ℓ^\perp as a function of z_*^\perp for different values of B . The red, green, blue, brown, orange, and cyan curves correspond to $B = 0, 0.1, 0.2, 0.3, 0.4,$ and 0.5 , respectively, in units of GeV.

The expression for the disconnected surface is again independent of the strip length ℓ^\perp and is now given by

$$S_{\text{discon}}^\perp = \frac{\ell_{y_1} \ell_{y_3} L^3}{2G_{(5)}} \left[\int_0^\infty dz \frac{e^{3A(z)} e^{B^2 z^2/2}}{z^3 \sqrt{g(z)}} \right]. \quad (29)$$

We can clearly see some differences in the above equations compared to the parallel case. Accordingly, some differences in the entanglement entropy result are also expected. The variation of ℓ^\perp with respect to the connected surface z_*^\perp for different values of B is shown in Fig. 7. We observe that for any given value of B , like in the parallel case, there is again a maximum length ℓ_{max}^\perp above which no connected solution exists and only the disconnected solution exists. However, as opposed to the parallel case, now not only the magnitude of ℓ_{max}^\perp but also the value of the turning point z_*^\perp at which it appears decreases with B . This suggests a lesser penetration of the entangling surface into the bulk as compared to the parallel case as B increases. Further, below ℓ_{max}^\perp , there are again two connected solutions (shown by solid and dashed lines) which can minimize the surface area. The solid line corresponds to the actual minima and appears for small z_*^\perp , whereas the dashed line corresponds to the saddle point and appears for large z_*^\perp .

The difference between the connected and disconnected entropies $\Delta S^\perp = S_{\text{con}}^\perp - S_{\text{discon}}^\perp$ for the perpendicular case is shown in Fig. 8 for various values of B . The connected solution with small z_*^\perp (indicated by solid lines) always has a lower entanglement entropy than the large- z_*^\perp solution (indicated by dashed lines). Further, ΔS^\perp goes from negative to positive values as ℓ^\perp increases, indicating that S_{con}^\perp (S_{discon}^\perp) minimizes the entropy for small ℓ^\perp (large ℓ^\perp). This results in a phase transition from connected to disconnected surfaces, similar to the ones in the parallel case, as we increase ℓ^\perp . The critical length at which this

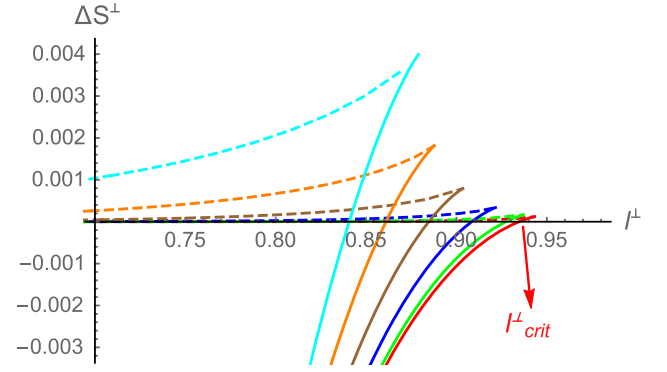


FIG. 8. $\Delta S^\perp = S_{\text{con}}^\perp - S_{\text{discon}}^\perp$ as a function of ℓ^\perp for different values of B . The red, green, blue, brown, orange, and cyan curves correspond to $B = 0, 0.1, 0.2, 0.3, 0.4,$ and 0.5 , respectively, in units of GeV.

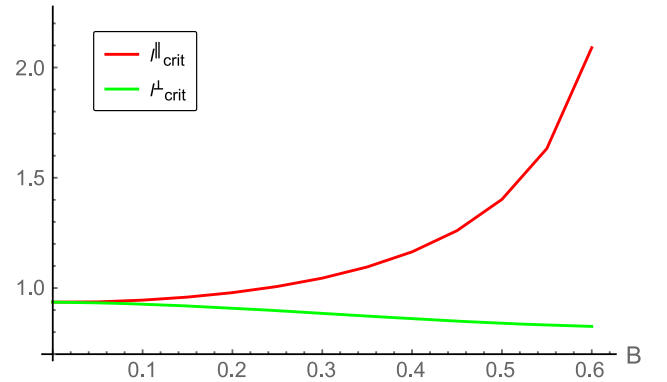


FIG. 9. Variation of ℓ_{crit}^\perp (green line) and $\ell_{\text{crit}}^\parallel$ (red line) as a function of B , in units of GeV.

phase transition appears is now defined as ℓ_{crit}^\perp , where $\ell_{\text{crit}}^\perp < \ell_{\text{max}}^\perp$. Therefore, similar to Eq. (26) for the parallel case, we again have a length scale at which the order of the entanglement entropy changes from $\mathcal{O}(N^2)$ to $\mathcal{O}(N^0)$. However, in contrast with the parallel case, this critical length in the perpendicular case now decreases with B . This is shown in Fig. 9, where the parallel-case result is also included for comparison. We find that the difference between $\ell_{\text{crit}}^\parallel - \ell_{\text{crit}}^\perp$ is small for small B ; however, it can be appreciable for large B . This suggests that the non-analyticity in the entanglement entropy appears at larger lengths in the parallel case compared to the perpendicular case for all values of B . Our whole analysis therefore suggests appreciable anisotropic changes in the entanglement entropy structure of the confined phase in the presence of a magnetic field.

B. Holographic mutual information

We now study the holographic mutual information with two strips in the confined phase. For simplicity, we concentrate only on equal-size strip subsystems

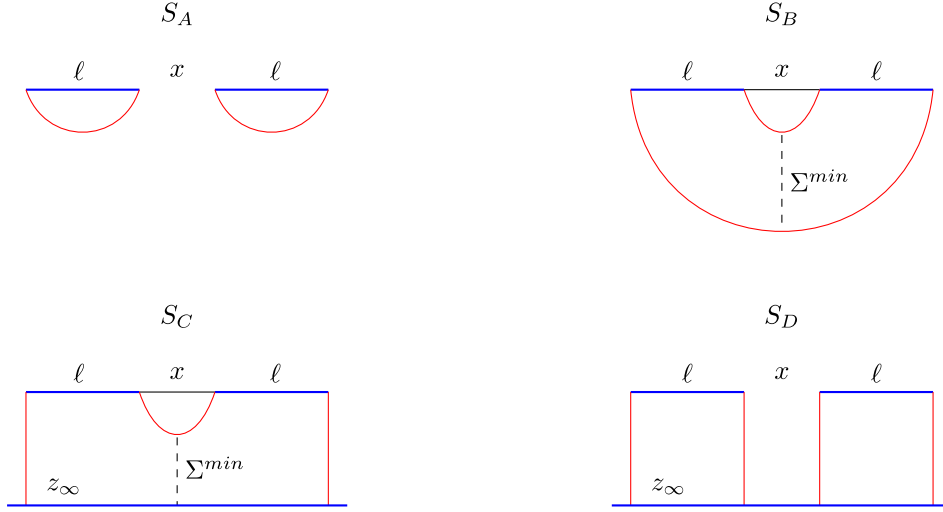


FIG. 10. Pictorial representation of the four different minimal surface configurations for the case of two strips of equal length ℓ separated by a distance x in the thermal-AdS background. The dashed line represents the entanglement wedge.

($\ell_1 = \ell_2 = \ell$), which are separated by a distance x . The entanglement structure with two subsystems is much more intriguing than that with one subsystem. In particular, depending on the magnitudes of ℓ and x , there can be four possible surfaces that minimize the entropy. These four surfaces are illustrated in Fig. 10. We can now have only connected surfaces (i.e., S_A and S_B), both connected and disconnected surfaces (S_C), or only the disconnected surface (S_D). The holographic entanglement entropies for these four configurations are as follows:

$$\begin{aligned}
 S_A(\ell, x) &= 2S_{\text{con}}(\ell), \\
 S_B(\ell, x) &= S_{\text{con}}(x) + S_{\text{con}}(2\ell + x), \\
 S_C(\ell, x) &= S_{\text{con}}(x) + S_{\text{discon}}, \\
 S_D(\ell, x) &= 2S_{\text{discon}},
 \end{aligned} \tag{30}$$

where S_{con} and S_{discon} are the single-interval holographic entanglement entropies for the connected and disconnected surfaces, respectively.

1. Parallel case

Let us first discuss the results when the strips are oriented in a parallel direction relative to the magnetic field. We find that there can be different phase transitions between the above-mentioned four configurations. This phase diagram can be illustrated better in the $(\ell^{\parallel}, x^{\parallel})$ plane and is shown in Fig. 11. We find that for small x^{\parallel} , $\ell^{\parallel} \ll \ell_{\text{crit}}^{\parallel}$, and the S_A phase is preferred as it has the lowest entropy. As ℓ^{\parallel} increases, the S_B phase becomes dominant. As we keep increasing ℓ^{\parallel} but keep $x^{\parallel} (\ll \ell_{\text{crit}}^{\parallel})$ fixed, a phase transition from S_B to S_C occurs. For $x^{\parallel} = 0$, this S_B -to- S_C phase transition happens at $\ell^{\parallel} = \ell_{\text{crit}}^{\parallel}/2$, whereas for a general

value of x^{\parallel} , it happens at $2\ell^{\parallel} + x^{\parallel} = \ell_{\text{crit}}^{\parallel}$. Further, if we take $x^{\parallel}, \ell^{\parallel} \gg \ell_{\text{crit}}^{\parallel}$, then the S_D configuration becomes the dominant one. We also observe that these phase transitions depend nontrivially on B . For example, the S_B/S_C phase transition line shifts to the right in the $\ell^{\parallel} - x^{\parallel}$ plane and appears for larger values of x^{\parallel} and ℓ^{\parallel} , whereas the S_A/S_C transition occurs for lower values of x^{\parallel} when B increases.

Also, there are two tricritical points in this phase diagram. For $B = 0.5$, these are indicated by two black dots. The first tricritical point is recognized when the S_A , S_B , and S_C phases coexist, and the second tricritical point occurs when the S_A , S_C , and S_D phases coexist. The presence of these phase transitions and critical points

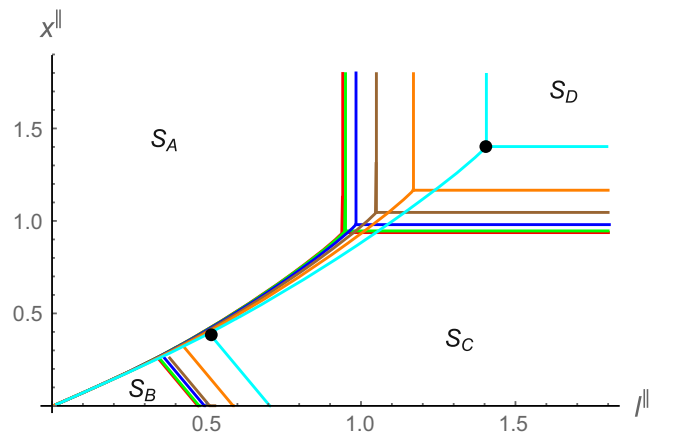


FIG. 11. Phase diagram of various minimal area surfaces for the case of two strips of equal length ℓ separated by a distance x in the confining background for the parallel case. The red, green, blue, brown, orange, and cyan curves correspond to $B = 0, 0.1, 0.2, 0.3, 0.4,$ and 0.5 , respectively. The two black dots indicate the two tricritical points for $B = 0.5$, in units of GeV.

reflects the nonanalytic nature of the entanglement entropy with multiple strips. The magnitudes of x^\parallel and ℓ^\parallel at these tricritical points also depend nontrivially on B and can be observed in Fig. 11.

It is also interesting to note that the order of the entanglement entropy (from N^2 to N^0 or vice versa) may or may not change as we pass through various phase transition lines in the two-strip case. For instance, there is no change in the order if the S_A , S_B , or S_C phases are involved, whereas the order can change if the S_D phase is involved.

Let us now address the holographic mutual information, $I = S_1 + S_2 - S_1 \cup S_2$, which in the above four different phases has the form

$$\begin{aligned}
 I_A(\ell^\parallel, x^\parallel) &= S_{\text{con}}^\parallel(\ell^\parallel) + S_{\text{con}}^\parallel(\ell^\parallel) - 2S_{\text{con}}^\parallel(\ell^\parallel) = 0, \\
 I_B(\ell^\parallel, x^\parallel) &= S_{\text{con}}^\parallel(\ell^\parallel) + S_{\text{con}}^\parallel(\ell^\parallel) - S_{\text{con}}^\parallel(x^\parallel) \\
 &\quad - S_{\text{con}}^\parallel(2\ell^\parallel + x^\parallel) \geq 0, \\
 I_C(\ell^\parallel, x^\parallel) &= S_{\text{con}}^\parallel(\ell^\parallel) + S_{\text{con}}^\parallel(\ell^\parallel) - S_{\text{con}}^\parallel(x^\parallel) \\
 &\quad - S_{\text{discon}}^\parallel \geq 0, \\
 I_D(\ell^\parallel, x^\parallel) &= S_{\text{discon}}^\parallel + S_{\text{discon}}^{EE} - 2S_{\text{discon}}^{EE} = 0,
 \end{aligned} \tag{31}$$

which in turn means that

$$\begin{aligned}
 \frac{\partial I_A}{\partial \ell^\parallel} &\propto \frac{1}{G_{(5)}^0} = \mathcal{O}(N^0), & \frac{\partial I_B}{\partial \ell^\parallel} &\propto \frac{1}{G_{(5)}} = \mathcal{O}(N^2), \\
 \frac{\partial I_C}{\partial \ell^\parallel} &\propto \frac{1}{G_{(5)}} = \mathcal{O}(N^2), & \frac{\partial I_D}{\partial \ell^\parallel} &\propto \frac{1}{G_{(5)}^0} = \mathcal{O}(N^0).
 \end{aligned} \tag{32}$$

Therefore, depending on the transition line, the order of the mutual information may or may not change as we go from one phase to another. For instance, going from the S_A phase to the S_B phase (by decreasing x^\parallel) causes a change in its order [from $\mathcal{O}(N^0)$ to $\mathcal{O}(N^2)$], whereas no such change occurs when we go from the S_B phase to the S_C phase (by increasing ℓ^\parallel).

The variation of the mutual information with respect to strip length ℓ^\parallel and separation length x^\parallel for different values of B is shown in Figs. 12 and 13. Here the mutual information in the S_B (S_C) phase is represented by the solid (dashed) lines. We observe that the mutual information varies smoothly as we move from S_B to S_C via the S_B/S_C transition line. In Fig. 12 we show the results for a fixed $x^\parallel = 0.2$ line, but similar results exist for other values of x^\parallel as well. As we increase B along the parallel direction, I_B almost remains the same but I_C increases slightly. Similarly, the mutual information smoothly goes to zero as we approach the S_A (or S_D) phase from the S_B (or S_C) phase. This is shown in Fig. 13.

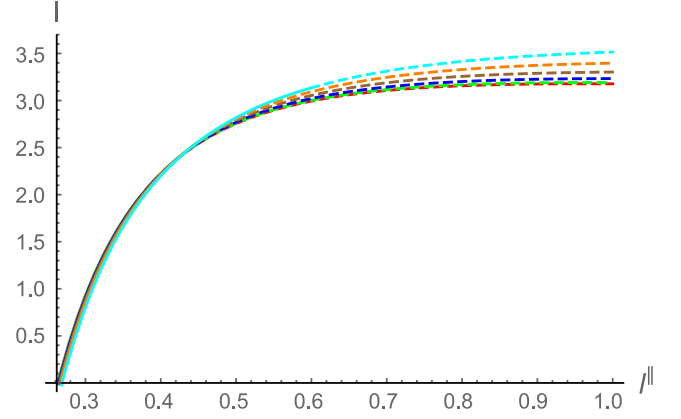


FIG. 12. Variation of the mutual information with ℓ^\parallel for different values of B . Here $x^\parallel = 0.2$ is used, and the red, green, blue, brown, orange, and cyan curves correspond to $B = 0, 0.1, 0.2, 0.3, 0.4,$ and 0.5 , respectively, in units of GeV.

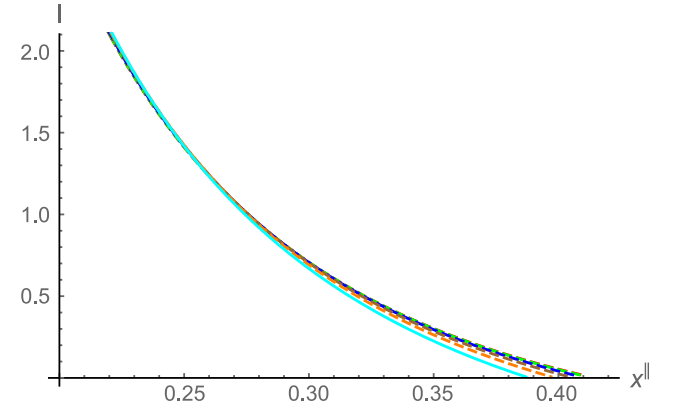


FIG. 13. Variation of the mutual information with x^\parallel for different values of B . Here $\ell^\parallel = 0.5$ is used, and the red, green, blue, brown, orange, and cyan curves correspond to $B = 0, 0.1, 0.2, 0.3, 0.4,$ and 0.5 , respectively, in units of GeV.

2. Perpendicular case

We now move on to discuss the two-strip phase diagram and the corresponding mutual information when the strips are oriented in the perpendicular direction. This phase diagram is shown in Fig. 14. We see that there are again four phases, with each one dominating different parts of the $\ell^\perp - x^\perp$ phase space, and they undergo various phase transitions as we vary ℓ^\perp and x^\perp . There are again two tricritical points, which are B dependent. This is qualitatively similar to the parallel-case phase diagram. However, there are some differences as well. In particular, the values of $\{\ell^\perp, x^\perp\}$ at both tricritical points now decrease with B , in contrast to the parallel case where these values at the second tricritical point increase with B . Similarly, in contrast to the parallel case, the size of the S_B phase now decreases for higher values of B . Moreover, the S_A/S_C transition line also moves slightly upward for higher values of B .

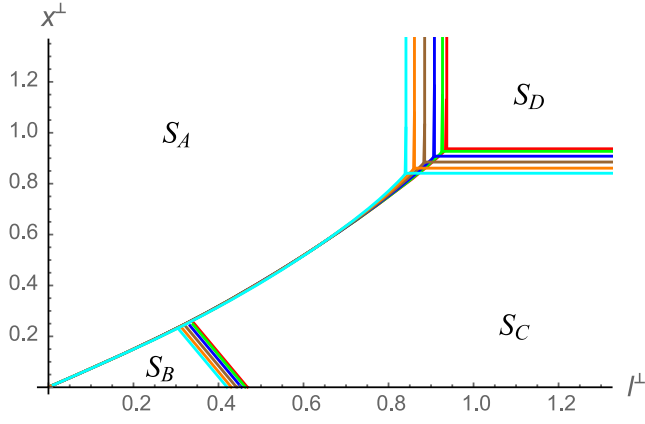


FIG. 14. Phase diagram of various minimal area surfaces for the case of two strips of equal length ℓ^\perp separated by a distance x^\perp in the confining background for the perpendicular case. The red, green, blue, brown, orange, and cyan curves correspond to $B = 0, 0.1, 0.2, 0.3, 0.4,$ and 0.5 , respectively, in units of GeV.

We can similarly compute the mutual information. The structure of the mutual information is qualitatively similar to the parallel case [Eq. (31)]. In particular, it goes to zero in the S_A and S_D phases, whereas it is finite and positive in the S_B and S_C phases. Therefore, it is again of order N^2 in the $\{S_B, S_C\}$ phases and is of order N^0 in the $\{S_A, S_D\}$ phases. The variation of the mutual information with ℓ^\perp for different values of B is shown in Fig. 15, where the solid and dashed lines are used to represent the mutual information in the S_B and S_C phases, respectively. We find that it varies smoothly as we move from the S_B phase to the S_C phase (or vice versa) via the S_B/S_C transition line. Further, the mutual information also varies smoothly with x^\perp and it goes to zero as the S_A or S_D phase is approached. This is shown in Fig. 16. This is consistent with the physical expectation that the entanglement between the

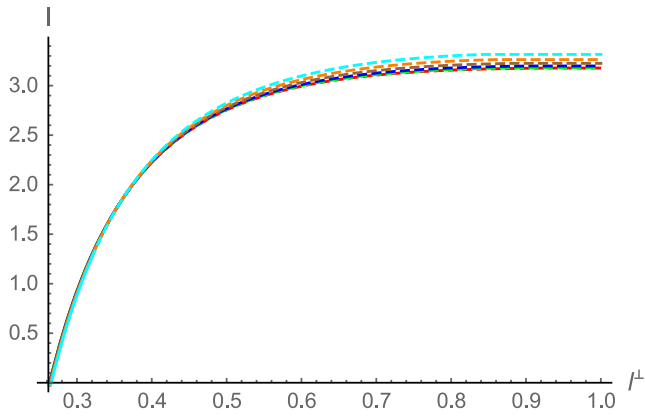


FIG. 15. Variation of the mutual information with ℓ^\perp for different values of B . Here $x^\perp = 0.2$ is used, and the red, green, blue, brown, orange, and cyan curves correspond to $B = 0, 0.1, 0.2, 0.3, 0.4,$ and 0.5 , respectively, in units of GeV.

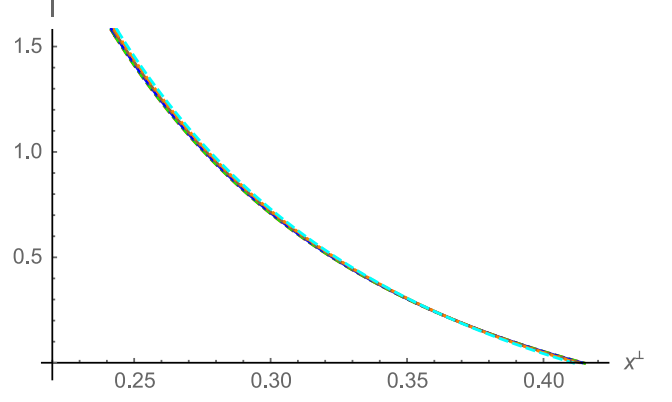


FIG. 16. Variation of the mutual information with x^\perp for different values of B . Here $\ell^\perp = 0.5$ is used, and the red, green, blue, brown, orange, and cyan curves correspond to $B = 0, 0.1, 0.2, 0.3, 0.4,$ and 0.5 , respectively, in units of GeV.

two subsystems should decrease when they are moved farther apart.

It is interesting to point out that, unlike the entanglement entropy, lattice results for the QCD mutual information are not available yet. These results from holography can have analogous correlations in real QCD, and therefore these results for the mutual information can be treated as a prediction from holography.

C. Entanglement wedge cross section

We now discuss the entanglement wedge cross section E_W in the confining phase. The surface that divides the entanglement wedge, associated with two strip subsystems A and B , into two parts can be identified as a vertical flat surface Σ from the symmetry consideration. Therefore, for the strip subsystems under consideration, E_W is given by the area of a constant y_1 (for the parallel case) or y_2 (for the perpendicular case) hypersurface located in the middle of the strips (see Fig. 10).

1. Parallel case

The entanglement wedge cross section in this case is given by the minimum area of the constant (y_1, t) hypersurface. The induced metric on this hypersurface is

$$(ds^2)_\Sigma^{\text{ind}} = \frac{L^2 e^{2A(z)}}{z^2} \left[\frac{dz^2}{g(z)} + e^{B^2 z^2} (dy_2^2 + dy_3^2) \right], \quad (33)$$

from which we obtain the entanglement wedge cross section as

$$E_W^\parallel = \frac{\ell_{y_2} \ell_{y_3} L^3}{4G_{(5)}} \left[\int dz \frac{e^{3A(z)} e^{B^2 z^2}}{z^3 \sqrt{g(z)}} \right]. \quad (34)$$

From the phase diagram, we can conclude that the entanglement wedge only exists for the S_B and S_C phases,

whereas it is zero in the S_A and S_D phases. For the S_B phase, it is given by

$$E_W^{\parallel}(S_B) = \frac{\ell_{y_2} \ell_{y_3} L^3}{4G_{(5)}} \left[\int_{z_*^{\parallel}(x)}^{z_*^{\parallel}(2\ell+x)} dz \frac{e^{3A(z)} e^{B^2 z^2}}{z^3 \sqrt{g(z)}} \right]. \quad (35)$$

Interestingly, the above integral can be evaluated explicitly as

$$\begin{aligned} &= \frac{\ell_{y_2} \ell_{y_3} L^3}{4G_{(5)}} \left[\frac{1}{2} (B^2 - 3a) Ei[(B^2 - 3a)z^2] \right. \\ &\quad \left. - \frac{e^{z^2(B^2-3a)}}{2z^2} \right]_{z=z_*^{\parallel}(x)}^{z=z_*^{\parallel}(2\ell+x)}, \end{aligned} \quad (36)$$

where Ei is the exponential integral function. Similarly, for the S_C phase, we have

$$\begin{aligned} E_W^{\parallel}(S_C) &= \frac{\ell_{y_2} \ell_{y_3} L^3}{4G_{(5)}} \left[\int_{z_*^{\parallel}(x)}^{\infty} dz \frac{e^{3A(z)} e^{B^2 z^2}}{z^3 \sqrt{g(z)}} \right] \\ &= -\frac{\ell_{y_2} \ell_{y_3} L^3}{4G_{(5)}} \left[\frac{1}{2} (B^2 - 3a) Ei[(B^2 - 3a)z^2] \right. \\ &\quad \left. - \frac{e^{z^2(B^2-3a)}}{2z^2} \right]_{z=z_*^{\parallel}(x)}. \end{aligned} \quad (37)$$

From the above results, it is clear that both $E_W^{\parallel}(S_B)$ and $E_W^{\parallel}(S_C)$ are not only positive as $z = z_*^{\parallel}(x) \leq z_*^{\parallel}(2\ell+x) \leq \infty$, but also UV finite. The analytic expressions of $E_W^{\parallel}(S_B)$ and $E_W^{\parallel}(S_C)$ further allow us to make several concrete observations about the entanglement wedge in the confining phase without resorting to any numerics. In particular, the difference between $E_W^{\parallel}(S_B) - E_W^{\parallel}(S_C)$, for the allowed range of the magnetic field

$$\begin{aligned} E_W^{\parallel}(S_B) - E_W^{\parallel}(S_C) &= \frac{\ell_{y_2} \ell_{y_3} L^3}{4G_{(5)}} \left[\frac{1}{2} (B^2 - 3a) Ei[(B^2 - 3a)z^2] \right. \\ &\quad \left. - \frac{e^{z^2(B^2-3a)}}{2z^2} \right]_{z=z_*^{\parallel}(2\ell+x)}, \end{aligned} \quad (38)$$

is always negative and finite at the S_B/S_C transition line (defined by $2\ell^{\parallel} + x^{\parallel} = \ell_{\text{crit}}^{\parallel}$). This indicates that, irrespective of the values of the magnetic field, the entanglement wedge cross section will exhibit a discontinuous behavior at the S_B/S_C transition line. This should be contrasted with the mutual information which behaves smoothly near this transition line. Similarly, since $z_*^{\parallel}(x) \neq \infty$, this implies that $E_W^{\parallel}(S_C)$ does not go to zero continuously as the S_C/S_D transition line is approached. The same is true for $E_W^{\parallel}(S_B)$, as it also does not go to zero when the S_A/S_B transition line

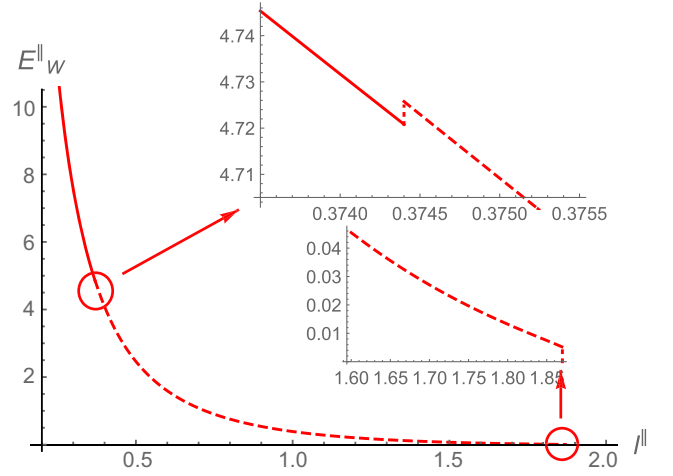


FIG. 17. E_W^{\parallel} as a function of separation length ℓ^{\parallel} along a fixed line $x^{\parallel} = 0.5\ell^{\parallel}$. Here $B = 0$ is used. Solid and dashed lines correspond to E_W^{\parallel} of the S_B and S_C phases, respectively, in units of GeV.

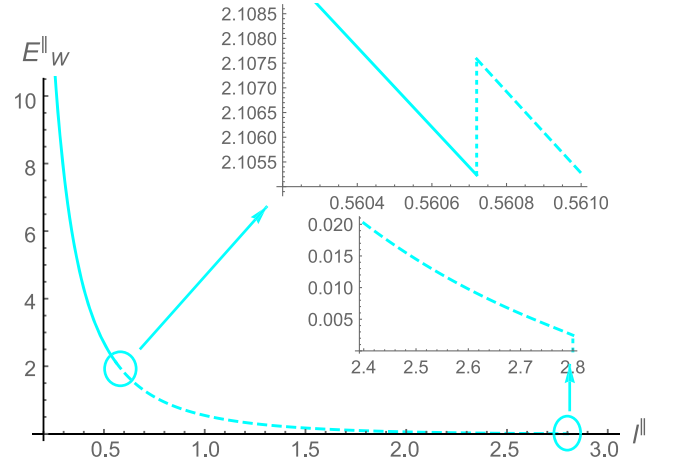


FIG. 18. E_W^{\parallel} as a function of separation length ℓ^{\parallel} along a fixed line $x^{\parallel} = 0.5\ell^{\parallel}$. Here $B = 0.5$ is used. Solid and dashed lines correspond to E_W^{\parallel} of the S_B and S_C phases, respectively, in units of GeV.

is approached [since $z_*^{\parallel}(x) \neq z_*^{\parallel}(2\ell^{\parallel} + x^{\parallel})$]. Therefore, we clearly see that, unlike the mutual information, the entanglement wedge exhibits discontinuity every time we pass through a transition line in the $\ell^{\parallel} - x^{\parallel}$ phase space.

Further details pertaining to the behavior of E_W^{\parallel} are summarized in Figs. 17 and 18 for two different values of B . Here, a particular line $x^{\parallel} = 0.5\ell^{\parallel}$ is considered so that the behavior of E_W^{\parallel} in the S_B , S_C , and S_D phases can be probed simultaneously. The solid and dashed lines are used to represent E_W^{\parallel} of the S_B and S_C phases, respectively.⁴

⁴In Figs. 17 and 18, the prefactor $\frac{\ell_{y_2} \ell_{y_3} L^3}{2G_{(5)}}$ is again set to one.

From the subplots, we clearly see that E_W^{\parallel} becomes discontinuous at the S_B/S_C transition line. Moreover, there is an upward jump in the magnitude of E_W^{\parallel} when the S_B/S_C transition line is approached from the S_B phase, i.e., $E_W^{\parallel}(S_C) > E_W^{\parallel}(S_B)$, indicating that the area of the wedge grows at this transition line. These results are in complete agreement with our analytical analysis. Similarly, $E_W^{\parallel}(S_C)$ does not go to zero at the S_C/S_D transition line, indicating that the entanglement wedge cross section vanishes abruptly for large values of ℓ^{\parallel} and x^{\parallel} . The same results are true for other values of B as well.

It is also interesting to see how the area of the entanglement wedge changes at the, e.g., S_B/S_C transition line for different values of B . This is shown in Fig. 19. We see that the difference $E_W^{\parallel}(S_C) - E_W^{\parallel}(S_B)$ is always positive at the transition point for all values of B . However, we further find that this difference decreases with B for relatively large B , suggesting a smaller discontinuity in the structure of E_W^{\parallel} at this transition line due to B . Moreover, the difference $E_W^{\parallel}(S_C) - E_W^{\parallel}(S_D)$ at the S_C/S_D transition line is found to be exactly similar to the behavior shown in Fig. 19. This can again be traced back to the fact that these differences depend only on the critical values $\ell_{\text{crit}}^{\parallel} (= x_{\text{crit}}^{\parallel})$ at the corresponding transition lines. On the other hand, the difference $E_W^{\parallel}(S_C) - E_W^{\parallel}(S_A)$ at the S_A/S_C transition line is found to be increasing with B for all values of x^{\parallel} and ℓ^{\parallel} , implying a strengthening of the wedge discontinuity at this transition line with B . This is shown in Fig. 20. Overall, we find that $E_W^{\parallel}(S_C)$ is a monotonically decreasing function of x^{\parallel} which abruptly vanishes at $x^{\parallel} = \ell_{\text{crit}}^{\parallel}$.

In holography, it has been suggested that the entanglement wedge always at least exceeds half the mutual information, i.e., $E_W^{\parallel} \geq I^{\parallel}/2$ [30]. Therefore, it is interesting to check if this inequality is satisfied in the current holographic model. The comparison between the

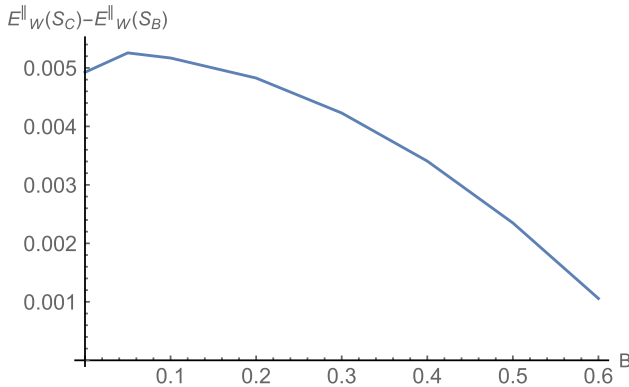


FIG. 19. Variation of $E_W^{\parallel}(S_C) - E_W^{\parallel}(S_B)$ with B at the S_B/S_C transition line along a fixed line $x^{\parallel} = 0.5\ell^{\parallel}$.

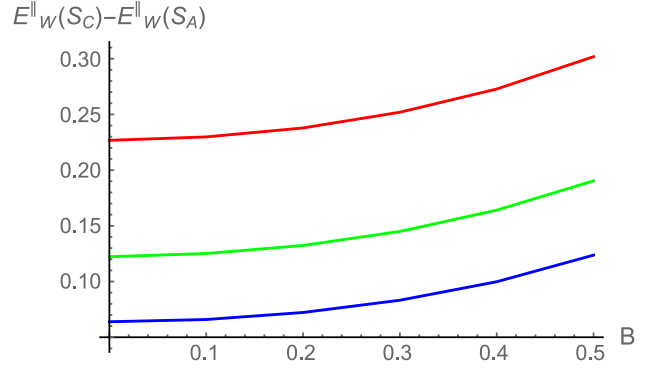


FIG. 20. Variation of $E_W^{\parallel}(S_C) - E_W^{\parallel}(S_A)$ with B at the S_C/S_A transition line. Here the red, green, and blue curves correspond to $x^{\parallel} = 0.5, 0.6,$ and $0.7,$ respectively.

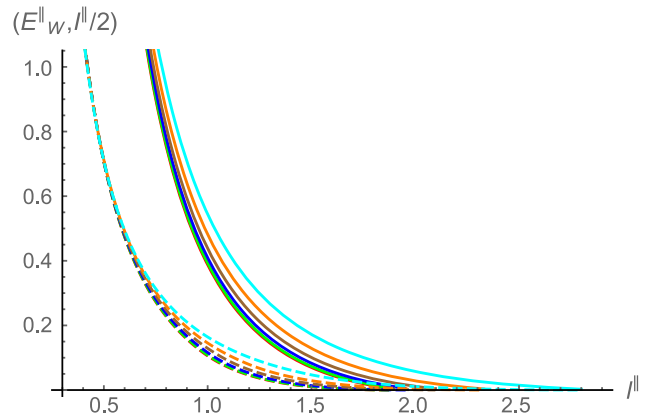


FIG. 21. Entanglement wedge E_W^{\parallel} and mutual information I^{\parallel} as functions of ℓ^{\parallel} along a fixed line $x^{\parallel} = 0.5\ell^{\parallel}$. The solid curves correspond to E_W^{\parallel} , whereas the dashed curves correspond to $I^{\parallel}/2$. The red, green, blue, brown, orange, and cyan curves correspond to $B = 0, 0.1, 0.2, 0.3, 0.4,$ and $0.5,$ respectively.

entanglement wedge and mutual information is shown in Fig. 21 along the line $x^{\parallel} = 0.5\ell^{\parallel}$ for different values of B . We find that, irrespective of the phases involved, this inequality is always satisfied for all values of B .

2. Perpendicular case

The computation of the entanglement wedge cross section E_W^{\perp} in the perpendicular direction is completely analogous to the parallel case. In this case, it is given by the minimum area of the constant (y_2, t) hypersurface. The induced metric on this hypersurface is

$$(ds^2)_{\Sigma}^{\text{ind}} = \frac{L^2 e^{2A(z)}}{z^2} \left[\frac{dz^2}{g(z)} + dy_1^2 + e^{B^2 z^2} (dy_3^2) \right], \quad (39)$$

from which the expression of the entanglement wedge cross section can be obtained as

$$E_W^\perp = \frac{\ell_{y_1} \ell_{y_3} L^3}{4G_{(5)}} \left[\int dz \frac{e^{3A(z)} e^{B^2 z^2/2}}{z^3 \sqrt{g(z)}} \right]. \quad (40)$$

The two-strip phase diagram of the perpendicular case again tells us that the nontrivial entanglement wedge can exist only in the S_B and S_C phases. For the S_B phase, we have

$$\begin{aligned} E_W^\perp(S_B) &= \frac{\ell_{y_1} \ell_{y_3} L^3}{4G_{(5)}} \left[\int_{z_*^\perp(x)}^{z_*^\perp(2\ell^\perp+x)} dz \frac{e^{3A(z)} e^{B^2 z^2/2}}{z^3 \sqrt{g(z)}} \right] \\ &= \frac{\ell_{y_1} \ell_{y_3} L^3}{4G_{(5)}} \left| \frac{1}{4} (B^2 - 6a) \text{Ei} \left[\frac{1}{2} (B^2 - 6a) z^2 \right] \right. \\ &\quad \left. - \frac{e^{\frac{1}{2} z^2 (B^2 - 6a)}}{2z^2} \right|_{z=z_*^\perp(x)}^{z=z_*^\perp(2\ell^\perp+x)}, \end{aligned} \quad (41)$$

whereas for S_C it is given by

$$\begin{aligned} E_W^\perp(S_C) &= \frac{\ell_{y_1} \ell_{y_3} L^3}{4G_{(5)}} \left[\int_{z_*^\perp(x)}^\infty dz \frac{e^{3A(z)} e^{B^2 z^2/2}}{z^3 \sqrt{g(z)}} \right] \\ &= -\frac{\ell_{y_1} \ell_{y_3} L^3}{4G_{(5)}} \left| \frac{1}{4} (B^2 - 6a) \text{Ei} \left[\frac{1}{2} (B^2 - 6a) z^2 \right] \right. \\ &\quad \left. - \frac{e^{\frac{1}{2} z^2 (B^2 - 6a)}}{2z^2} \right|_{z=z_*^\perp(x)}. \end{aligned} \quad (42)$$

The variation of E_W^\perp with ℓ^\perp along the line $x^\perp = 0.5\ell^\perp$ for two different values of B is shown in Figs. 22 and 23. We find that the behavior of E_W^\perp is qualitatively similar to the parallel case. In particular, E_W^\perp again behaves discontinuously at the S_B/S_C transition line. This can be seen mathematically from Eqs. (41) and (42), where the

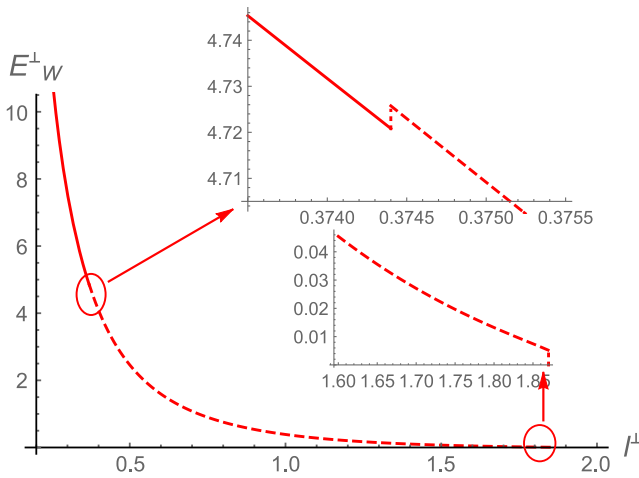


FIG. 22. E_W^\perp as a function of separation length ℓ^\perp along a fixed line $x^\perp = 0.5\ell^\perp$. Here $B = 0$ is used. Solid and dashed lines correspond to E_W^\perp of the S_B and S_C phases, respectively, in units of GeV.

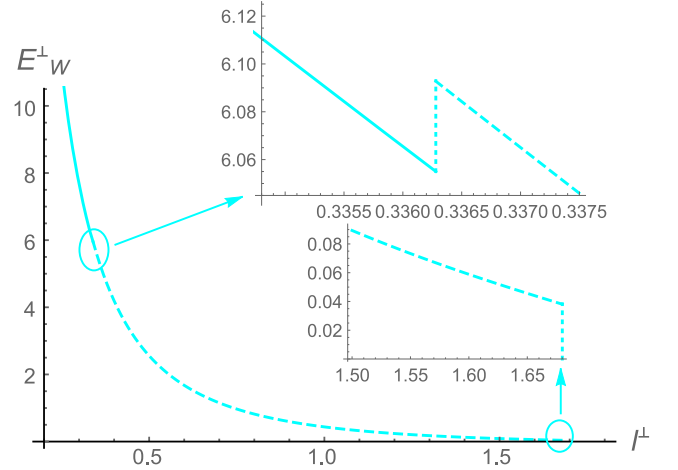


FIG. 23. E_W^\perp as a function of separation length ℓ^\perp along a fixed line $x^\perp = 0.5\ell^\perp$. Here $B = 0.5$ is used. Solid and dashed lines correspond to E_W^\perp of the S_B and S_C phases, respectively, in units of GeV.

condition $z_*^\perp(2\ell^\perp + x^\perp) \neq \infty$ ensures that $E_W^\perp(S_B)$ and $E_W^\perp(S_C)$ do not attain the same value at the S_B/S_C transition line. Moreover, the entanglement wedge does not vanish smoothly as the S_A (or S_D) phase is approached from the S_B (or S_C) phase. This result can again be traced back to the fact that $z_*^\perp(x^\perp) \neq z_*^\perp(2\ell^\perp + x^\perp) \neq \infty$. Accordingly, we find that the entanglement wedge is a monotonic function of x^\perp , which vanishes discontinuously at $x^\perp = \ell_{\text{crit}}^\perp$. Therefore, like in the parallel case, the entanglement wedge exhibits discontinuity each time a phase transition between different phases occurs in the perpendicular case as well.

We can further analyze how much the area of the entanglement wedge changes at the transition point in the perpendicular case. At the S_B/S_C transition line, this is shown in Fig. 24. This can be compared with Fig. 19 of the parallel case. We find that the difference between $E_W^\perp(S_C) - E_W^\perp(S_B)$ is always positive [since $z_*^\perp(x^\perp) < z_*^\perp(2\ell^\perp + x^\perp)$], suggesting an increment in the area of

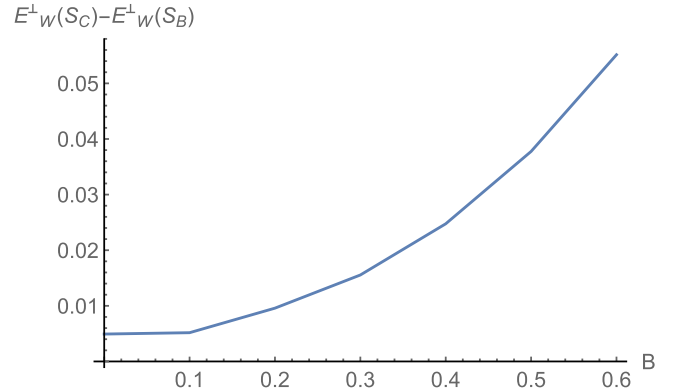


FIG. 24. Variation of $E_W^\perp(S_C) - E_W^\perp(S_B)$ with B at the S_B/S_C transition line along a fixed line $x^\perp = 0.5\ell^\perp$.

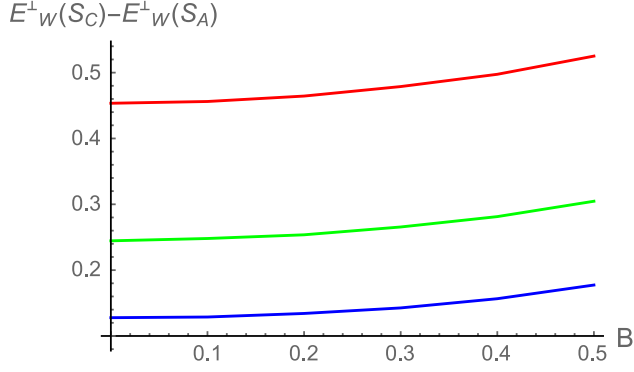


FIG. 25. Variation of $E_W^\perp(S_C) - E_W^\perp(S_A)$ with B at the S_C/S_A transition line. Here the red, green, and blue curves correspond to $x^\perp = 0.5, 0.6, \text{ and } 0.7$, respectively.

the entanglement wedge at the transition point. This result is similar to the parallel case. However, in contrast to the parallel case, the difference $E_W^\perp(S_C) - E_W^\perp(S_B)$ increases with B . This points to a larger discontinuity in the entanglement wedge cross section at the S_B/S_C transition point with B in the perpendicular direction. Similarly, the difference $E_W^\perp(S_C) - E_W^\perp(S_A)$ at the S_A/S_C transition line is found to be an increasing function of B for all values of x^\perp and ℓ^\perp . This behavior is quite similar to the parallel case, though the magnitude of the difference is slightly higher now. This is shown in Fig. 25.

We further test the inequality $E_W^\perp \geq I^\perp/2$ in the perpendicular case. The results are shown in Fig. 26. We find that this inequality is again satisfied everywhere in the $\ell^\perp - x^\perp$ plane for all values of B . The inequality saturates only at the critical points, at which $I^\perp/2$ continuously goes to zero, whereas E_W^\perp exhibits a sharp drop to zero.

From the above analysis, we see that the entanglement wedge not only exhibits nontrivial features each time a

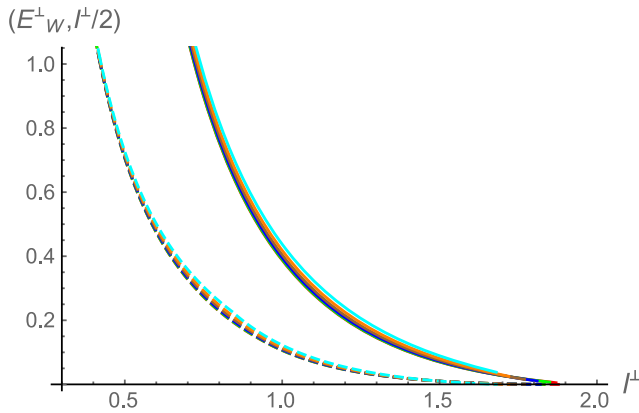


FIG. 26. Entanglement wedge E_W^\perp and mutual information I^\perp as functions of ℓ^\perp along a fixed line $x^\perp = 0.5\ell^\perp$. The solid curves correspond to E_W^\perp , whereas the dashed curves correspond to $I^\perp/2$. The red, green, blue, brown, orange, and cyan curves correspond to $B = 0, 0.1, 0.2, 0.3, 0.4, \text{ and } 0.5$, respectively.

phase transition between different phases occurs but also is sensitive to the orientation of the magnetic field. This is an important result considering that the entanglement wedge has been suggested as the holographic dual of many mixed-state entanglement measures. Therefore, our whole analysis suggests that nontrivial and anisotropic features are expected in these measures in the presence of a magnetic field, especially in the confined phase.

D. Holographic entanglement negativity

We now study the holographic entanglement negativity in the confined phase. We begin with the single-interval case. This is given in Eq. (21). In the limit $B \rightarrow A^c \rightarrow \infty$, the disconnected entropy dominates for both the parallel and perpendicular cases (see Fig. 3 for more details). So for both cases, we have

$$\begin{aligned} \mathcal{E} &= \lim_{B \rightarrow A^c} \frac{3}{4} [2S(A) + S(B_1) + S(B_2) \\ &\quad - S(A \cup B_1) - S(A \cup B_2)], \\ \mathcal{E} &= \frac{3}{2} S(A). \end{aligned} \quad (43)$$

This is an interesting new result implying that the holographic entanglement negativity is just $3/2$ times the entanglement entropy in the single-interval case. This suggests that the entanglement negativity is also discontinuous at the critical lengths $\ell_{\text{crit}}^\parallel$ (ℓ_{crit}^\perp) for the parallel (perpendicular) case. Therefore, the entanglement negativity also undergoes an order change from $\mathcal{O}(N^2)$ to $\mathcal{O}(N^0)$ at these critical lengths. For instance, for the parallel case, we have

$$\begin{aligned} \frac{\partial \mathcal{E}^\parallel}{\partial \ell^\parallel} &= \mathcal{O}(N^2) \quad \text{for } \ell^\parallel < \ell_{\text{crit}}^\parallel, \\ \frac{\partial \mathcal{E}^\parallel}{\partial \ell^\parallel} &= \mathcal{O}(N^0) \quad \text{for } \ell^\parallel > \ell_{\text{crit}}^\parallel, \end{aligned} \quad (44)$$

with similar results for the perpendicular case. The discontinuous aspect of \mathcal{E} in the confined phase is an interesting new result and a prediction from holography (strictly speaking, a prediction from the entanglement negativity proposal of Refs. [34,35]) and should be amenable for independent testing. Here, we further find that this discontinuous behavior of \mathcal{E} in the confined phase persists in the presence of a magnetic field as well. Moreover, the direction and B dependence of the critical lengths associated with the negativity remain the same as that illustrated in Fig. 9, implying that the magnetic field induces orientation-dependent features in this particular entanglement measure as well.

We now proceed to discuss the holographic entanglement negativity when we have two disjoint intervals

[40,42]. In comparison to Refs. [40,42], in our case we have $l_s = x, l_1 = l_2 = \ell$. Hence, \mathcal{E} is expressed as

$$\mathcal{E} = \frac{3}{4} [S(\ell + x) + S(\ell + x) - S(2\ell + x) - S(x)], \quad (45)$$

wherein S denotes the holographic entanglement entropy for a single interval. If $x > \ell_{\text{crit}}$, then $\mathcal{E} = 0$ in Eq. (45) as all terms are now dominated by the disconnected entropy S_{discon} . This implies that, just like the mutual information and entanglement wedge, \mathcal{E} is zero in the S_D phase as well. This is true for both the parallel and perpendicular cases. However, as we will see shortly, the entanglement negativity does not vanish in the S_A phase.

1. Negativity for two strips in the parallel direction

The variation of \mathcal{E}^{\parallel} with x^{\parallel} for two strips is shown in Fig. 27. Here $\ell^{\parallel} = 0.8$ is used for illustration, but similar results exist for other values of ℓ^{\parallel} as well. We find that \mathcal{E}^{\parallel} varies monotonically with x^{\parallel} and smoothly approaches zero at $x^{\parallel} = \ell_{\text{crit}}^{\parallel}$. In particular, as is expected, the negativity decreases as the two subsystems are taken further and further apart, and eventually vanishes. An interesting result to note is that \mathcal{E}^{\parallel} is finite in some parts of the S_A phase. This is in sharp contrast to the behavior of the mutual information and entanglement wedge, which was zero everywhere in the S_A phase. Only when $x^{\parallel} \geq \ell_{\text{crit}}^{\parallel}$ does the negativity go to zero in the S_A phase.

We further find that \mathcal{E}^{\parallel} also varies monotonically with ℓ^{\parallel} . This is shown in Fig. 28. Here we use a fixed $x^{\parallel} = 0.1$ line such that all three phases can be simultaneously probed. We observe that as we increase B , the value of \mathcal{E}^{\parallel} increases for all three phases $\{S_A, S_B, S_C\}$. We find that the negativity first increases as the size of the

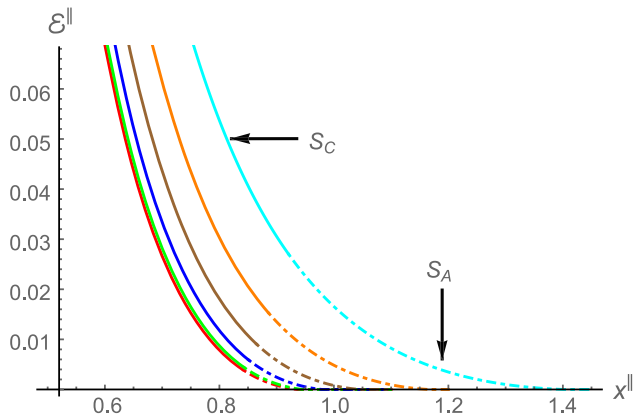


FIG. 27. \mathcal{E}^{\parallel} as a function of length x^{\parallel} for different values of B . Here $\ell^{\parallel} = 0.8$ is used. The dot-dashed and solid lines correspond to \mathcal{E}^{\parallel} of the S_A and S_C phases, respectively. The red, green, blue, brown, orange, and cyan curves correspond to $B = 0, 0.1, 0.2, 0.3, 0.4,$ and 0.5 , respectively, in units of GeV.

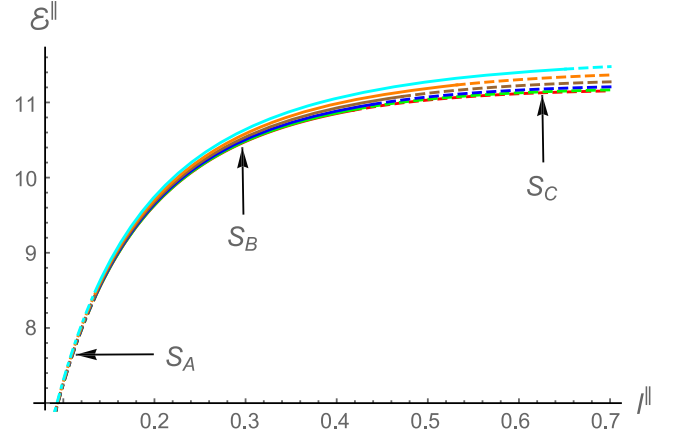


FIG. 28. \mathcal{E}^{\parallel} as a function of length ℓ^{\parallel} for different values of B . Here $x^{\parallel} = 0.1$ is used. The dot-dashed, solid, and dashed lines correspond to \mathcal{E}^{\parallel} of the $S_A, S_B,$ and S_C phases, respectively. The red, green, blue, brown, orange, and cyan curves correspond to $B = 0, 0.1, 0.2, 0.3, 0.4,$ and 0.5 , respectively, in units of GeV.

subsystems increases and then saturates to a B -dependent constant value. This B -dependent constant value, in particular, increases as B increases. Moreover, our analysis further suggests that, unlike the entanglement wedge, the entanglement negativity behaves smoothly across various phase transition lines and there is no discontinuity in its structure.

2. Negativity for two strips in the perpendicular direction

The negativity results for two strips in the perpendicular direction are shown in Figs. 29 and 30. The results are again qualitatively similar to the parallel case. The negativity again decreases monotonically with separation size and only goes to zero at the critical separation length $x^{\perp} = \ell_{\text{crit}}^{\perp}$,

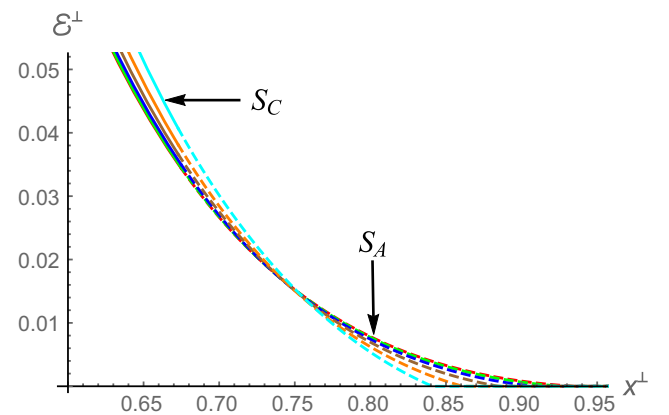


FIG. 29. \mathcal{E}^{\perp} as a function of length x^{\perp} for different values of B . Here $\ell^{\perp} = 0.7$ is used. The dot-dashed and solid lines correspond to \mathcal{E}^{\perp} of the S_A and S_C phases, respectively. The red, green, blue, brown, orange, and cyan curves correspond to $B = 0, 0.1, 0.2, 0.3, 0.4,$ and 0.5 , respectively, in units of GeV.

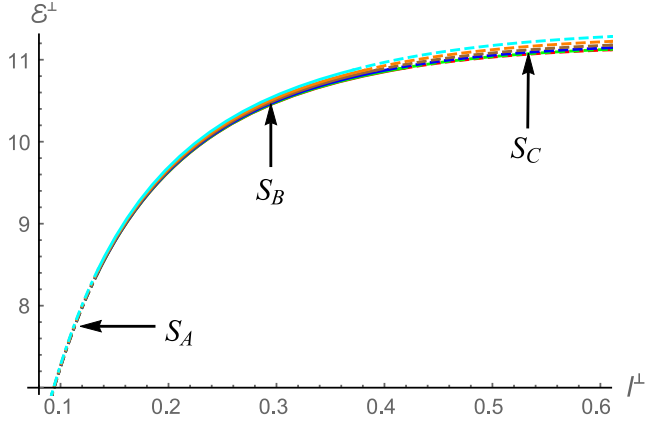


FIG. 30. \mathcal{E}^\perp as a function of length ℓ^\perp for different values of B . Here $x^\perp = 0.1$ is used. The dot-dashed, solid, and dashed lines correspond to \mathcal{E}^\perp of the S_A , S_B , and S_C phases, respectively. The red, green, blue, brown, orange, and cyan curves correspond to $B = 0, 0.1, 0.2, 0.3, 0.4$, and 0.5 , respectively, in units of GeV.

and thus it is again nonzero in some parts of the S_A phase. We further observe that as we increase B along the perpendicular direction, the value of \mathcal{E}^\perp initially increases and then decreases. In particular, the negativity always increases with B in the S_C phase; however, in the S_A phase it increases with B for small x^\perp , whereas it decreases with B near x_{crit}^\perp . This behavior is different from the parallel case wherein only the increment in negativity was observed. Similarly, we observe that \mathcal{E}^\perp first monotonically increases with ℓ^\perp and then saturates to a B -dependent constant value. This B -dependent constant value, like in the parallel case, increases with B . Importantly, \mathcal{E}^\perp is again continuous across various phase transitions.

We end this section by making a few observations about the entanglement negativity. As mentioned in the last section, there are two different holographic proposals for the entanglement negativity. In the first proposal [32,33], the negativity is proportional to the entanglement wedge (neglecting the quantum correction term). Since the entanglement wedge is zero in the S_A and S_D phases, this suggests that the negativity, if computed using the proposal of Refs. [32,33], would also be zero in these phases. However, as discussed above, the second proposal of Refs. [34,35] gives a nonzero negativity in some parts of the S_A phase. Therefore, as far as the negativity for two strips in the confined phase is concerned, these two proposals seem to provide inequivalent results. It should be mentioned that both of these proposals have been tested for conformal field theories and have independently reproduced exact known results for the negativity. Therefore, our results provide the first counterexample where the disparity between these two proposals is observed. Also, as we will see shortly, a similar feature is present for all values of the magnetic field and temperature in the deconfined phase, suggesting that the proposal of Refs. [34,35] points

to some kind of universality in the structure of the entanglement negativity.

V. DECONFINING PHASE

Having thoroughly discussed the various holographic entanglement measures in the confined phase, we now proceed to discuss them in the finite-temperature deconfined phase. This corresponds to having a black hole on the dual gravity side. Apart from the magnetic field, we also have another parameter, i.e., temperature, in the theory. There is again an option of aligning the strip subsystems parallel or perpendicular to the magnetic field.

A. Holographic entanglement entropy

We start by studying the entanglement entropy for a single interval where the boundary subsystem can be aligned parallel or perpendicular to the magnetic field in a fashion similar to the thermal-AdS case. In the AdS black hole background, we again have two types of solutions for the entanglement entropy: connected and disconnected [139]. The disconnected entropy, however, turns out to be always higher than the connected entropy. The expressions of the connected entropy and strip length are the same as in the thermal-AdS case, except that $g(z)$ is now given by Eq. (4). So, for the parallel direction, we have Eqs. (23) and (24) for the connected entanglement entropy and strip length, whereas analogous equations for the perpendicular direction are given in Eqs. (27) and (28).

The entanglement entropy of the disconnected surface, however, will get an additional contribution. In the parallel direction we have

$$S_{\text{discon}}^{\parallel} = \frac{\ell_{y_2} \ell_{y_3} L^3}{2G_{(5)}} \left[\int_0^{z_h} dz \frac{e^{3A(z)} e^{B^2 z^2}}{z^3 \sqrt{g(z)}} + \frac{e^{3A(z_h) B^2 z_h^2}}{2z_h^3} \ell^{\parallel} \right], \quad (46)$$

and for the perpendicular direction we have

$$S_{\text{discon}}^{\perp} = \frac{\ell_{y_1} \ell_{y_3} L^3}{2G_{(5)}} \left[\int_0^{z_h} dz \frac{e^{3A(z)} e^{B^2 z^2/2}}{z^3 \sqrt{g(z)}} + \frac{e^{3A(z_h) + B^2 z_h^2}}{2z_h^3} \ell^{\perp} \right], \quad (47)$$

where the last terms in both the parallel and perpendicular cases come from the surface along the horizon at $z = z_h$.

We now proceed to discuss the numerical results for the entanglement entropy in the deconfined phase. The variation of the strip length with respect to the turning point of the connected surface at two different temperatures $T = 1.5T_{\text{crit}}$ and $2.0T_{\text{crit}}$ for different values of B is shown in Fig. 31 for the parallel case and in Fig. 32 for the perpendicular case. We observe that for both orientations there exist certain common features. To begin with, unlike in the confined phase, there is no $\ell_{\text{max}}^{\parallel}$ or $\ell_{\text{max}}^{\perp}$ and the

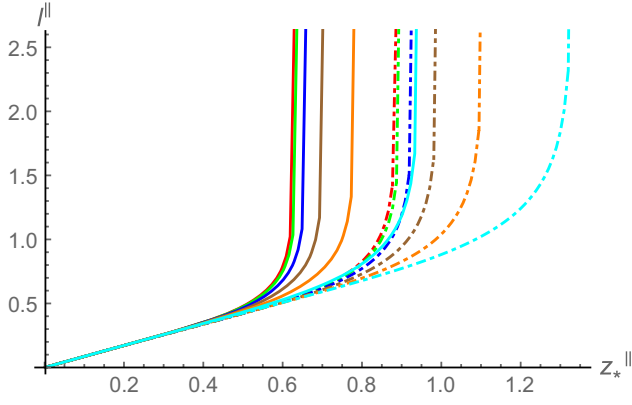


FIG. 31. ℓ^{\parallel} as a function of z_*^{\parallel} for different values of magnetic field and temperature. The red, green, blue, brown, orange, and cyan curves correspond to $B = 0, 0.1, 0.2, 0.3, 0.4,$ and 0.5 , respectively. Dot-dashed and solid lines correspond to $T/T_{\text{crit}} = 1.5$ and 2.0 , respectively, in units of GeV.

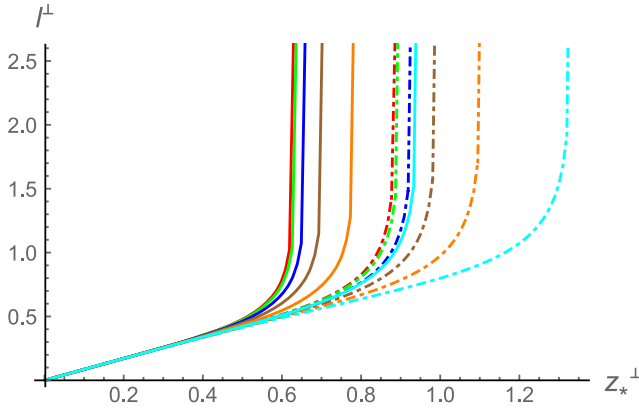


FIG. 32. ℓ^{\perp} as a function of z_*^{\perp} for different values of magnetic field and temperature. The red, green, blue, brown, orange, and cyan curves correspond to $B = 0, 0.1, 0.2, 0.3, 0.4,$ and 0.5 , respectively. Dot-dashed and solid lines correspond to $T/T_{\text{crit}} = 1.5$ and 2.0 , respectively, in units of GeV.

connected solution exists for the entire strip length. Second, as we increase the strip length, the connected surface's turning point moves closer to the horizon. Last, as we increase B , for a given value of the strip length, the value of the turning point increases. These observations imply that, irrespective of the orientation of the strip, the strip goes deeper into the bulk by increasing B . This result is in contrast to the confining-phase results wherein the orientation of the magnetic field does induce anisotropy.

The corresponding entanglement entropy behavior is shown in Figs. 33 and 34 for the parallel and perpendicular cases, respectively. We again see common features for both orientations. First, we see that there is no $\ell_{\text{crit}}^{\parallel}$ (or $\ell_{\text{crit}}^{\perp}$) for the parallel (or perpendicular) case and therefore no phase transition is observed from a connected to a disconnected surface on increasing the strip length in both cases. Next, we see that for both orientations, the difference

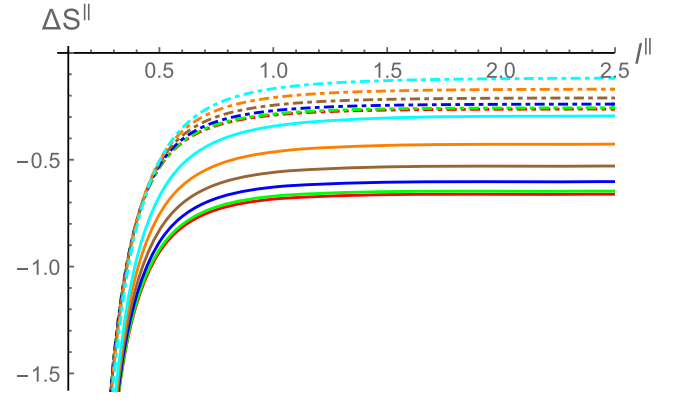


FIG. 33. $\Delta S^{\parallel} = S_{\text{con}}^{\parallel} - S_{\text{discon}}^{\parallel}$ as a function of ℓ^{\parallel} for different values of magnetic field and temperature. The red, green, blue, brown, orange, and cyan curves correspond to $B = 0, 0.1, 0.2, 0.3, 0.4,$ and 0.5 , respectively. Dot-dashed and solid lines correspond to $T/T_{\text{crit}} = 1.5$ and 2.0 , respectively, in units of GeV.

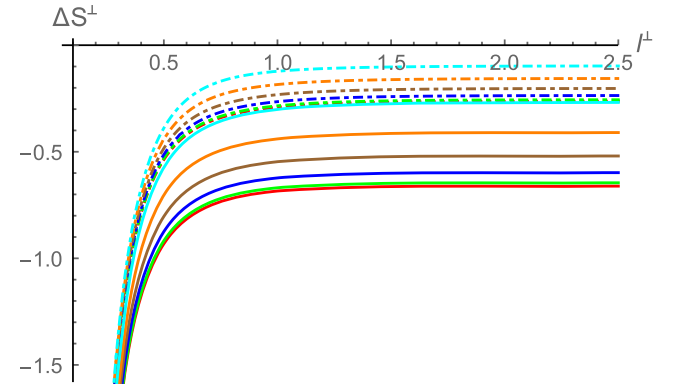


FIG. 34. $\Delta S^{\perp} = S_{\text{con}}^{\perp} - S_{\text{discon}}^{\perp}$ as a function of ℓ^{\perp} for different values of magnetic field and temperature. The red, green, blue, brown, orange, and cyan curves correspond to $B = 0, 0.1, 0.2, 0.3, 0.4,$ and 0.5 , respectively. Dot-dashed and solid lines correspond to $T/T_{\text{crit}} = 1.5$ and 2.0 , respectively, in units of GeV.

in the entropy is always less than zero, implying that the connected entropy is always less than the disconnected entropy. Further, in the limit $\ell^{\parallel} \rightarrow \infty$, we have

$$S_{\text{con}}^{\parallel} = S_{\text{discon}}^{\parallel} = S_{\text{BH}} = \frac{V_3 e^{3A(z_h) + B^2 z_h^2}}{4G_{(5)} z_h^3}. \quad (48)$$

Similarly, in the limit $\ell^{\perp} \rightarrow \infty$, we have

$$S_{\text{con}}^{\perp} = S_{\text{discon}}^{\perp} = S_{\text{BH}} = \frac{V_3 e^{3A(z_h) + B^2 z_h^2}}{4G_{(5)} z_h^3}, \quad (49)$$

where the S_{BH} represents the Bekenstein-Hawking entropy of the AdS black hole. This reproduces the expected result that the entanglement entropy reduces to the thermal entropy when the size of the subsystem goes to infinity.

So, effectively, the entanglement entropy in the deconfined phase is always of order N^2 ,

$$\frac{\partial S^{\parallel}}{\partial \ell^{\parallel}} \propto \frac{1}{G_{(5)}} = \mathcal{O}(N^2), \quad \frac{\partial S^{\perp}}{\partial \ell^{\perp}} \propto \frac{1}{G_{(5)}} = \mathcal{O}(N^2). \quad (50)$$

Essentially, the behavior of the entanglement entropy remains qualitatively the same for both the parallel and perpendicular cases in the deconfined phase.

B. Two-strip phase diagram and mutual information

Since there is no phase transition between connected and disconnected entanglement entropies, the corresponding two-strip phase diagram in the deconfined phase is much simpler. Here, we only have two phases S_A and S_B as the connected surface dominates for any given strip length. Therefore, in the phase diagram, as shown for the parallel orientation in Fig. 35 and for the perpendicular orientation in Fig. 36, we can only see the phase transition between the S_A and S_B phases. We observe that the S_A phase is preferred when x^{\parallel} (or x^{\perp}) is large, while the S_B phase is preferred for large ℓ^{\parallel} (or ℓ^{\perp}). We further observe that on increasing B , the parameter space of the S_B phase increases, suggesting its preference over the S_A phase for larger magnetic field values. This is true for both the parallel and perpendicular cases. We again see that, although the magnetic field does introduce substantial changes in the phase diagram, these changes are qualitatively similar for the parallel and perpendicular cases, suggesting limited orientational effects of B in the deconfined phase. Similarly, for a fixed B , the phase space of S_B is found to increase with temperature.

The mutual information in the S_A and S_B phases displays similar features as in the confined phase. This is shown in

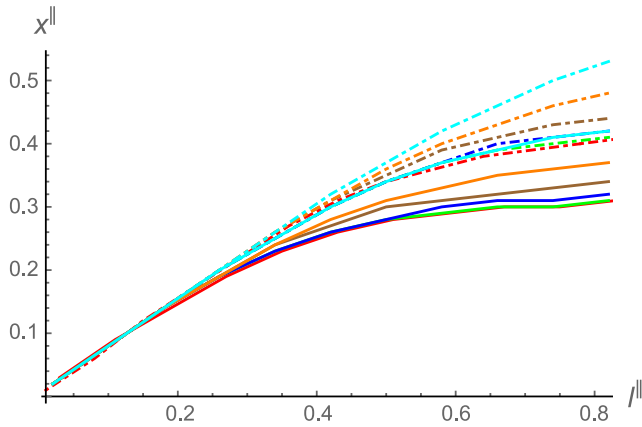


FIG. 35. Two-strip phase diagram in the deconfining background for the parallel case for different values of magnetic field and temperature. The red, green, blue, brown, orange, and cyan curves correspond to $B = 0, 0.1, 0.2, 0.3, 0.4,$ and 0.5 , respectively. Dot-dashed and solid lines correspond to $T/T_{\text{crit}} = 1.5$ and 2.0 respectively. In units of GeV.

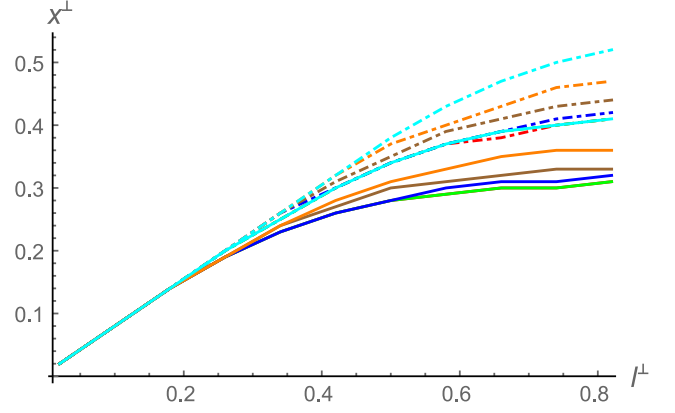


FIG. 36. Two-strip phase diagram in the deconfining background for the perpendicular case for different values of magnetic field and temperature. The red, green, blue, brown, orange, and cyan curves correspond to $B = 0, 0.1, 0.2, 0.3, 0.4,$ and 0.5 , respectively. Dot-dashed and solid lines correspond to $T/T_{\text{crit}} = 1.5$ and 2.0 , respectively, in units of GeV.

Figs. 37 and 38 for the parallel and perpendicular cases, respectively. The mutual information is zero in the S_A phase, whereas it is a monotonically increasing function of strip length in the S_B phase. Moreover, the behavior of the mutual information as a function of separation length is similar to the ones shown in Fig. 13, and therefore we do not present it here for brevity. In particular, it is a monotonically decreasing function of the separation length and it goes to zero in a smooth fashion as we pass from the S_B phase to the S_A phase. Therefore, an order change in the mutual information appears during the S_A/S_B phase transition as $I_A \propto \mathcal{O}(N^0)$ and $I_B \propto \mathcal{O}(N^2)$. This behavior is again true for both the parallel and perpendicular orientations.

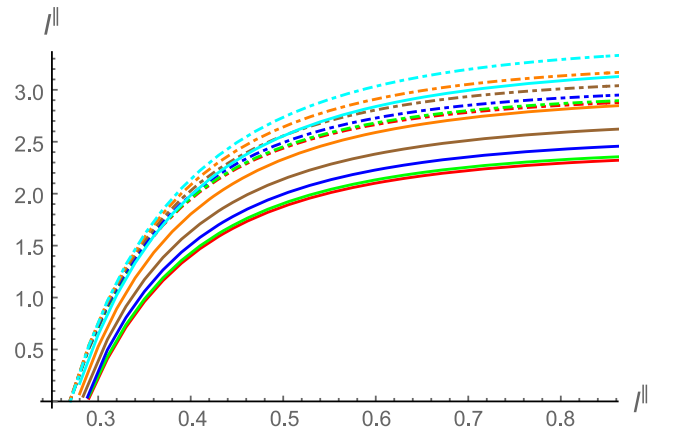


FIG. 37. I^{\parallel} as a function of ℓ^{\parallel} for different values of magnetic field and temperature. Here $x^{\parallel} = 0.2$ is used. The red, green, blue, brown, orange, and cyan curves correspond to $B = 0, 0.1, 0.2, 0.3, 0.4,$ and 0.5 , respectively. Dot-dashed and solid lines correspond to $T/T_{\text{crit}} = 1.5$ and 2.0 , respectively, in units of GeV.

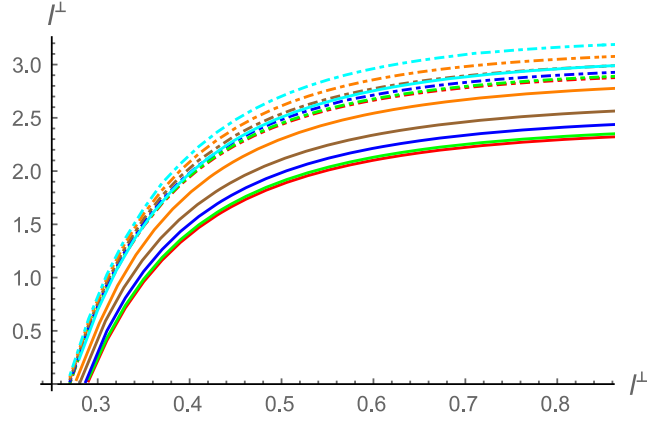


FIG. 38. I^\perp as a function of ℓ^\perp for different values of magnetic field and temperature. Here $x^\perp = 0.2$ is used. The red, green, blue, brown, orange, and cyan curves correspond to $B = 0, 0.1, 0.2, 0.3, 0.4,$ and 0.5 , respectively. Dot-dashed and solid lines correspond to $T/T_{\text{crit}} = 1.5$ and 2.0 , respectively, in units of GeV.

C. Entanglement wedge cross section

We now move on to discuss the entanglement wedge cross section E_W in the deconfining phase. Guided by the symmetry of the configuration (see Fig. 2), the area of the vertical surface Σ_{AB}^{min} gives the entanglement wedge cross section. In the case of an AdS black hole, E_W exists only for the S_B phase and its expression is similar to the thermal-AdS case, except that $g(z)$ is now given by Eq. (4). Therefore, for the parallel orientation we have

$$E_W^\parallel(S_B) = \frac{\ell_{y_1} \ell_{y_2} \ell_{y_3} L^3}{4G_{(5)}} \left[\int_{z_*^\parallel(x)}^{z_*^\parallel(2\ell+x)} dz \frac{e^{3A(z)} e^{B^2 z^2}}{z^3 \sqrt{g(z)}} \right]. \quad (51)$$

Similarly, for the perpendicular orientation we have

$$E_W^\perp(S_B) = \frac{\ell_{y_1} \ell_{y_2} \ell_{y_3} L^3}{4G_{(5)}} \left[\int_{z_*^\perp(x)}^{z_*^\perp(2\ell+x)} dz \frac{e^{3A(z)} e^{B^2 z^2/2}}{z^3 \sqrt{g(z)}} \right]. \quad (52)$$

Since no wedge exists between two subsystems in the S_A phase, accordingly the entanglement wedge cross section is zero in this phase.

The behavior of E_W as a function of strip length for different values of magnetic field and temperature is shown in Figs. 39 and 40 for the parallel and perpendicular cases, respectively. Here we choose a fixed separation length x^\parallel (or x^\perp) = 0.2 for illustration purposes, but similar results exist for other values of x^\parallel (or x^\perp) as well. The nature of E_W is again qualitatively similar in both orientations. In particular, the magnitude of E_W increases with B in both cases. However, the increment is slightly higher in the parallel case compared to the perpendicular case. E_W again turns out to be a monotonic function of strip length in the S_B phase, which vanishes discontinuously in the S_A phase.

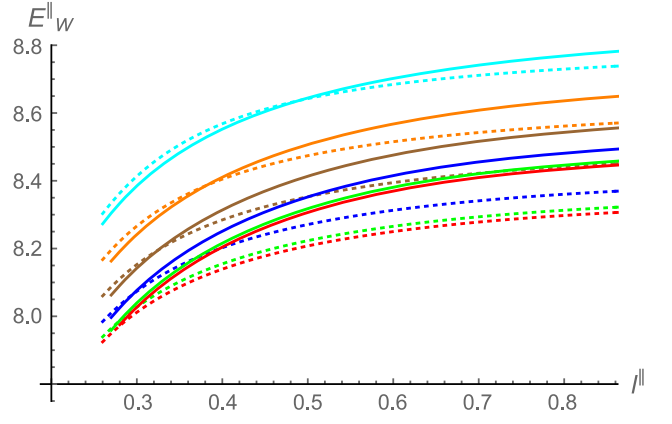


FIG. 39. E_W^\parallel as a function of ℓ^\parallel for different values of magnetic field and temperature. Here $x^\parallel = 0.2$ is used. The red, green, blue, brown, orange, and cyan curves correspond to $B = 0, 0.1, 0.2, 0.3, 0.4,$ and 0.5 , respectively. Dotted and solid lines correspond to $T/T_{\text{crit}} = 1.5$ and 2.0 , respectively, in units of GeV.

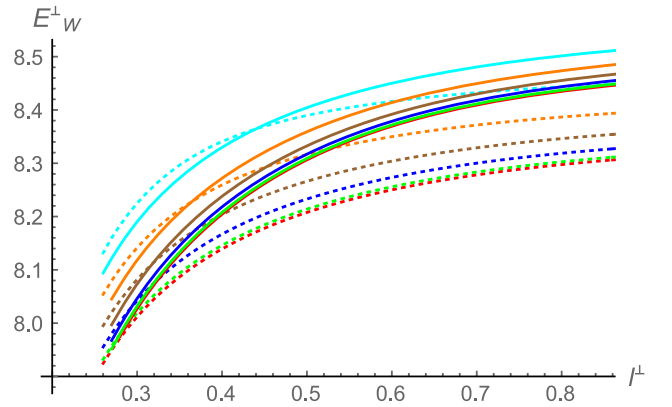


FIG. 40. E_W^\perp as a function of ℓ^\perp for different values of magnetic field and temperature. Here $x^\perp = 0.2$ is used. The red, green, blue, brown, orange, and cyan curves correspond to $B = 0, 0.1, 0.2, 0.3, 0.4,$ and 0.5 , respectively. Dotted and solid lines correspond to $T/T_{\text{crit}} = 1.5$ and 2.0 , respectively, in units of GeV.

This is true for all temperatures and magnetic fields. Further, in the presence of B , the thermal profile of E_W exhibits an interesting feature, i.e., E_W decreases with temperature for small trip lengths, whereas it increases with temperature for large strip lengths. This novel feature appears only in the presence of B and is true for both the parallel and perpendicular cases.

Similarly, E_W is also a monotonic function of the separation length. This is shown in Figs. 41 and 42 for the parallel and perpendicular cases, respectively. For both cases, like in the confined phase, E_W decreases with the separation length in the S_B phase and discontinuously becomes zero as we enter the S_A phase. We find that this discontinuous behavior of E_W at the S_A/S_B transition line is true for all values of magnetic field and temperature.

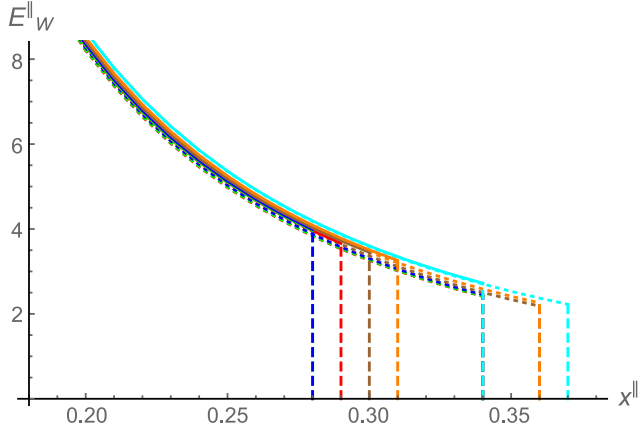


FIG. 41. E_W^{\parallel} as a function of x^{\parallel} for different values of magnetic field and temperature. Here $\ell^{\parallel} = 0.5$ is used. The red, green, blue, brown, orange, and cyan curves correspond to $B = 0, 0.1, 0.2, 0.3, 0.4,$ and 0.5 , respectively. Dotted and solid lines correspond to $T/T_{\text{crit}} = 1.5$ and 2.0 , respectively, in units of GeV.

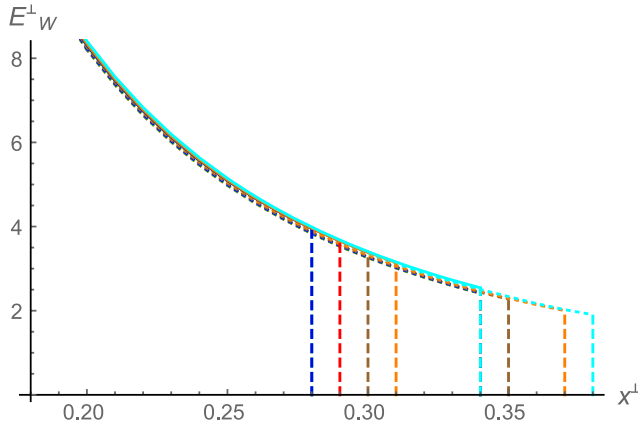


FIG. 42. E_W^{\perp} as a function of x^{\perp} for different values of magnetic field and temperature. Here $\ell^{\perp} = 0.5$ is used. The red, green, blue, brown, orange, and cyan curves correspond to $B = 0, 0.1, 0.2, 0.3, 0.4,$ and 0.5 , respectively. Dotted and solid lines correspond to $T/T_{\text{crit}} = 1.5$ and 2.0 , respectively, in units of GeV.

We further test (although not explicitly shown here) the inequality $E_W \geq I/2$ in the deconfined phase and find that this inequality is again satisfied everywhere in the $\ell - x$ plane of the parallel and perpendicular orientations for all values of magnetic field and temperature. The inequality saturates only at the S_A/S_B transition line, at which $I/2$ continuously goes to zero, whereas E_W exhibits a sharp drop to zero.

D. Holographic entanglement negativity

In this subsection, we talk about the holographic entanglement negativity in the deconfined phase. Beginning with the single-interval case, wherein the holographic negativity is given by Eq. (21), we have in the limit $B \rightarrow A^c \rightarrow \infty$

$$\begin{aligned} \mathcal{E} &= \lim_{B \rightarrow A^c} \frac{3}{4} [2S(A) + S(B_1) + S(B_2) \\ &\quad - S(A \cup B_1) - S(A \cup B_2)], \\ \mathcal{E} &= \frac{3}{2} S(A) \end{aligned} \quad (53)$$

as, apart from S_A , the rest of the four terms represent the same quantity in the limit $B \rightarrow A^c \rightarrow \infty$, i.e., the black hole entropy, and therefore cancel each other. Accordingly, in the single-interval case, we have $\mathcal{E} = \frac{3}{2} S_A$ irrespective of the orientation of the magnetic field. This is the same result that we got in the confined phase as well. Therefore, for a single-interval case, the negativity in the confined and deconfined phases is always $3/2$ times the entanglement entropy. Accordingly,

$$\frac{\partial \mathcal{E}}{\partial \ell} \propto \frac{1}{G_N} = \mathcal{O}(N^2). \quad (54)$$

The negativity is always of order $\mathcal{O}(N^2)$ in the deconfined phase for both parallel and perpendicular magnetic fields. This is different from the confined phase, where the negativity undergoes an order change at some critical strip length.

Moving on to the two-disjoint-interval case, we have the entanglement negativity as [40,42]

$$\mathcal{E} = \frac{3}{4} [S(\ell + x) + S(\ell + x) - S(2\ell + x) - S(x)], \quad (55)$$

where S denotes the holographic entanglement entropy for a single interval. Notice that, as is expected, when $x \rightarrow \infty$, i.e., for large separations, the negativity goes to zero as all terms in the above equation represent the black hole entropy. Interestingly, like in the confined case, there can be some region in the parameter space of the S_A phase where the negativity is nonzero. This once again has to be contrasted with the mutual information and entanglement wedge of the deconfined phase where these quantities were zero everywhere in the S_A phase. Indeed, as shown in Figs. 43 and 44 for the parallel and perpendicular cases, respectively, the negativity is nonzero in the S_A phase as well. The nonzero negativity for large separations in the deconfined phase is again an important prediction (again, strictly speaking, a prediction of the negativity proposal of Refs. [40,42]). Moreover, the negativity turns out to be a monotonic function of both strip length and separation length; in particular, it decreases for higher separation lengths, whereas it increases for higher strip lengths. We further find that for a fixed strip length and separation length the negativity increases slightly with higher magnetic fields, whereas thermal effects try to decrease it. These results are again qualitatively similar for both the parallel and perpendicular cases.

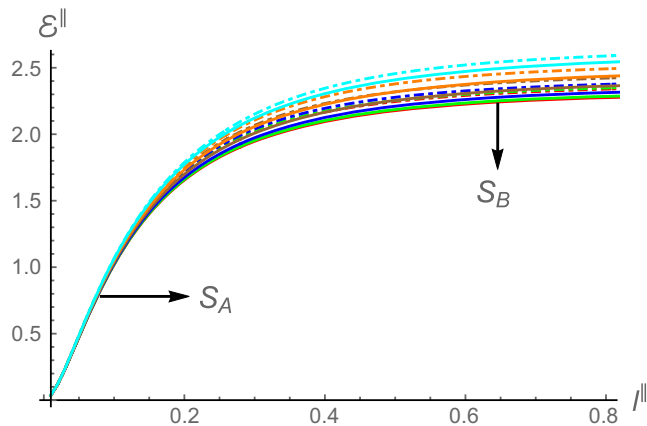


FIG. 43. \mathcal{E}^{\parallel} as a function of ℓ^{\parallel} for different values of magnetic field and temperature. Here $x^{\parallel} = 0.2$ is used. The red, green, blue, brown, orange, and cyan curves correspond to $B = 0, 0.1, 0.2, 0.3, 0.4,$ and 0.5 , respectively. Dot-dashed and solid lines correspond to $T/T_{\text{crit}} = 1.5$ and 2.0 , respectively, in units of GeV.

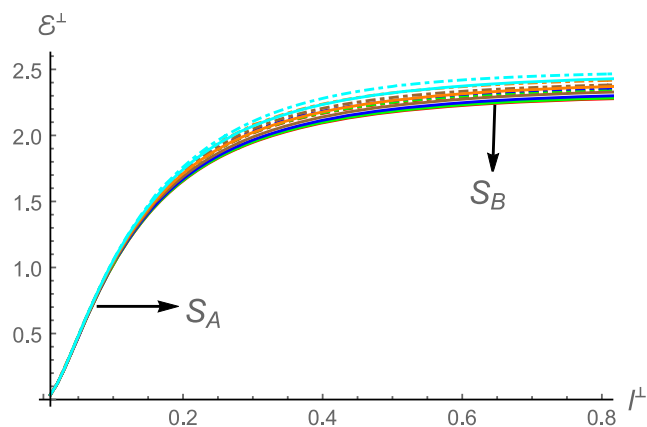


FIG. 44. \mathcal{E}^{\perp} as a function of ℓ^{\perp} for different values of magnetic field and temperature. Here $x^{\perp} = 0.2$ is used. The red, green, blue, brown, orange, and cyan curves correspond to $B = 0, 0.1, 0.2, 0.3, 0.4,$ and 0.5 , respectively. Dot-dashed and solid lines correspond to $T/T_{\text{crit}} = 1.5$ and 2.0 , respectively, in units of GeV.

We end this section by mentioning that our investigation suggests that the orientation-dependent effects of the magnetic field in the high-temperature deconfined phase are rather limited compared to the low-temperature confined phase. Though some nontrivial changes do arise in various entanglement measures between parallel and transverse magnetic fields in the deconfined phase, these changes are not as substantial as in the confined phase. For example, the magnetic field produced distinct effects in the entanglement phase diagram of the confined phase in the parallel and transverse directions, whereas the phase diagram is quite similar for both orientations in the deconfined phase. In the deconfined phase, the anisotropic effects might be suppressed by the large thermal effects. Indeed, if we do a large-temperature expansion of the

entanglement entropy and strip length, the effect of the magnetic field appears in a similar fashion for both orientations.

VI. DISCUSSION AND CONCLUSION

In this work, we performed a comprehensive analysis of the effects of a background magnetic field on various pure and mixed entanglement measures in the holographic confined/deconfined phases dual to a bottom-up phenomenological Einstein-Maxwell-dilaton gravity model. The magnetic field is expected to play an important role in QCD-related physics and here we analyzed in detail how this magnetic field alters the structure of the entanglement entropy, mutual information, entanglement wedge cross section, and entanglement negativity, in the confined/deconfined phases of QCD.

We first reestablished the known results of the entanglement entropy of a single strip in the confining phase, but now in the presence of a magnetic field. In particular, a phase transition from connected to disconnected entanglement entropy is observed at some critical strip length in the confined phase, at which the order of the entanglement entropy changes from $\mathcal{O}(N^2)$ to $\mathcal{O}(N^0)$. Interestingly, this critical length is found to increase/decrease for parallel/perpendicular magnetic fields, thereby providing anisotropic imprints of the magnetic field on the entanglement structure. We then analyzed the two-equal-strip entanglement phase diagram in the parameter space of strip length ℓ and separation length x and found four distinct phases $\{S_A, S_B, S_C, S_D\}$. These four phases exchange dominance as x and ℓ are varied, leading to an interesting phase diagram. This two-strip phase diagram is again greatly modified in the presence of a magnetic field, while further exhibiting anisotropic features. The mutual information turned out to be nonzero only in the S_B and S_C phases and is always a monotonic function of x and ℓ . Similarly, the entanglement wedge cross section E_W was found to be nonzero only in the S_B and S_C phases. Interestingly, unlike the mutual information, E_W vanishes discontinuously for large values of x and ℓ and exhibits nonanalytic behavior across various transition lines. In particular, going from the S_B phase to the S_C phase, E_W increases at the S_B/S_C transition line. Interestingly, this increment in the area of the entanglement wedge at the S_B/S_C transition line is found to decrease/increase for magnetic fields in parallel/perpendicular directions, yielding yet another anisotropic feature in the entanglement structure. Moreover, we tested the inequality concerning the mutual information and E_W and found that the latter always exceeds half of the former everywhere in the $\ell - x$ parameter space for all values of B . Similarly, we analyzed the behavior of the entanglement negativity with one and two intervals using the holographic proposal suggested in Refs. [34,35] and found many interesting features in the confined phase. For a single-strip subsystem, the negativity turned out to be just $3/2$

times the entanglement entropy, implying that it also undergoes an order change, from $\mathcal{O}(N^2)$ to $\mathcal{O}(N^0)$, as the strip length is varied. This suggests that it can also be used, like the entanglement entropy, to probe confinement. The corresponding critical length is further found to increase/decrease for parallel/perpendicular magnetic fields. Moreover, for two strips, the negativity behaves smoothly across various phase transition lines and no discontinuity in its structure is realized. However, unlike the mutual information and entanglement wedge, the negativity can be nonzero in some parts of the S_A phase, an interesting feature that may not be observed in the holographic negativity proposal of Refs. [32,33]. In addition, the negativity was found to display anisotropic features in parallel and perpendicular directions.

We then analyzed the entanglement structure of the deconfined phase. We found that there is no connected/disconnected transition and the entanglement entropy is always given by the connected surface. Accordingly, the two-strip phase diagram is much simpler in the deconfined phase. In particular, there are now only phases (S_A and S_B), with mutual information and entanglement wedge nonzero only in the S_B phase, whereas the entanglement negativity can be nonzero in both the S_A and S_B phases. We further found that the parameter space of the S_B phase increases for both orientations of the magnetic field, suggesting a larger phase space for the nontrivial entanglement wedge in the presence of a magnetic field. Similarly, the entanglement negativity of a single strip was again found to be proportional to the entanglement entropy, whereas for two strips it was found to be a monotonic function of x and ℓ for all values of magnetic field and temperature. Our analysis suggests that, although the magnetic field introduces substantial changes in the entanglement measures, these changes remain qualitatively similar in both the parallel and perpendicular cases, suggesting a limited anisotropic effect

of the magnetic field in the deconfined phase as compared to the confined phase.

We end this discussion by mentioning a few directions to extend our work. The next step in our research setup would be to include the chemical potential, as it also plays an important role in QCD physics, and to simultaneously discuss the effects of magnetic field and chemical potential on the entanglement structure of confined/deconfined phases. In the simplistic situation, this can be done in the current holographic setup as well by adding another gauge field on the gravity side. Similarly, it would also be interesting to compute E_W and \mathcal{E} after a global quantum quench and analyze the thermalization process via these measures, as this might also provide important information about the formation of quark-gluon plasma in QCD. We hope to come back to these issues in the near future.

ACKNOWLEDGMENTS

We would like to thank D. Choudhuri for careful reading of the paper and pointing out the necessary corrections. The work of P. J. has been supported by an appointment to the Junior Research Groups Program at the Asia Pacific Center for Theoretical Physics through the Science and Technology Promotion Fund and Lottery Fund of the Korean Government. P. J. is also supported by the Korean Local Governments—Gyeongsangbuk-do Province and Pohang City—and by the National Research Foundation of Korea (NRF) funded by the Korean government (MSIT) (Grant No. 2021R1A2C1010834). The work of S. S. J. is supported by Grant No. 09/983(0045)/2019-EMR-I from Council of Scientific & Industrial Research-Human Resource Development Group (CSIR-HRDG), India. The work of S. M. is supported by the Department of Science and Technology, Government of India under the Grant Agreement No. IFA17-PH207 (INSPIRE Faculty Award).

-
- [1] J. M. Maldacena, The large N limit of superconformal field theories and supergravity, *Int. J. Theor. Phys.* **38**, 1113 (1999); *Adv. Theor. Math. Phys.* **2**, 231 (1998).
 - [2] S. S. Gubser, I. R. Klebanov, and A. M. Polyakov, Gauge theory correlators from noncritical string theory, *Phys. Lett. B* **428**, 105 (1998).
 - [3] E. Witten, Anti-de Sitter space and holography, *Adv. Theor. Math. Phys.* **2**, 253 (1998).
 - [4] I. R. Klebanov, D. Kutasov, and A. Murugan, Entanglement as a probe of confinement, *Nucl. Phys.* **B796**, 274 (2008).
 - [5] T. Nishioka and T. Takayanagi, AdS bubbles, entropy and closed string tachyons, *J. High Energy Phys.* **01** (2007) 090.
 - [6] G. Vidal, J. I. Latorre, E. Rico, and A. Kitaev, Entanglement in Quantum Critical Phenomena, *Phys. Rev. Lett.* **90**, 227902 (2003).
 - [7] T. J. Osborne and M. A. Nielsen, Entanglement in a simple quantum phase transition, *Phys. Rev. A* **66**, 032110 (2002).
 - [8] L. Bombelli, R. K. Koul, J. Lee, and R. D. Sorkin, A quantum source of entropy for black holes, *Phys. Rev. D* **34**, 373 (1986).
 - [9] M. Srednicki, Entropy and Area, *Phys. Rev. Lett.* **71**, 666 (1993).
 - [10] H.-K. Lo, Classical communication cost in distributed quantum information processing—a generalization of quantum communication complexity, *Phys. Rev. A* **62**, 012313 (2000).

- [11] E. Karpov, D. Daems, and N.J. Cerf, Entanglement enhanced classical capacity of quantum communication channels with correlated noise in arbitrary dimensions, *Phys. Rev. A* **74**, 032320 (2006).
- [12] S. Ryu and T. Takayanagi, Holographic Derivation of Entanglement Entropy from AdS/CFT, *Phys. Rev. Lett.* **96**, 181602 (2006).
- [13] S. Ryu and T. Takayanagi, Aspects of holographic entanglement entropy, *J. High Energy Phys.* **08** (2006) 045.
- [14] F. Pastawski, B. Yoshida, D. Harlow, and J. Preskill, Holographic quantum error-correcting codes: Toy models for the bulk/boundary correspondence, *J. High Energy Phys.* **06** (2015) 149.
- [15] P. Hayden, S. Nezami, X.L. Qi, N. Thomas, M. Walter, and Z. Yang, Holographic duality from random tensor networks, *J. High Energy Phys.* **11** (2016) 009.
- [16] C.V. Johnson, Large N phase transitions, finite volume, and entanglement entropy, *J. High Energy Phys.* **03** (2014) 047.
- [17] A. Dey, S. Mahapatra, and T. Sarkar, Thermodynamics and entanglement entropy with Weyl corrections, *Phys. Rev. D* **94**, 026006 (2016).
- [18] A. Dey, S. Mahapatra, and T. Sarkar, Very general holographic superconductors and entanglement thermodynamics, *J. High Energy Phys.* **12** (2014) 135.
- [19] M. Van Raamsdonk, Building up spacetime with quantum entanglement, *Gen. Relativ. Gravit.* **42**, 2323 (2010); *Int. J. Mod. Phys. D* **19**, 2429 (2010).
- [20] V. Balasubramanian, B.D. Chowdhury, B. Czech, J. de Boer, and M.P. Heller, Bulk curves from boundary data in holography, *Phys. Rev. D* **89**, 086004 (2014).
- [21] V. Balasubramanian, A. Bernamonti, J. de Boer, N. Copland, B. Craps, E. Keski-Vakkuri, B. Muller, A. Schafer, M. Shigemori, and W. Staessens, Holographic thermalization, *Phys. Rev. D* **84**, 026010 (2011).
- [22] H. Liu and S.J. Suh, Entanglement Tsunami: Universal Scaling in Holographic Thermalization, *Phys. Rev. Lett.* **112**, 011601 (2014).
- [23] A. Dey, S. Mahapatra, and T. Sarkar, Holographic thermalization with Weyl corrections, *J. High Energy Phys.* **01** (2016) 088.
- [24] G. Vidal and R.F. Werner, Computable measure of entanglement, *Phys. Rev. A* **65**, 032314 (2002).
- [25] R. Horodecki, P. Horodecki, M. Horodecki, and K. Horodecki, Quantum entanglement, *Rev. Mod. Phys.* **81**, 865 (2009).
- [26] B.M. Terhal, M. Horodecki, D.W. Leung, and D.P. DiVincenzo, The entanglement of purification, *J. Math. Phys. (N.Y.)* **43**, 4286 (2002).
- [27] J. Eisert and M.B. Plenio, A comparison of entanglement measures, *J. Mod. Opt.* **46**, 145 (1999).
- [28] M. Horodecki, P. Horodecki, and R. Horodecki, Separability of mixed states: Necessary and sufficient conditions, *Phys. Lett. A* **223**, 1 (1996).
- [29] A. Peres, Separability Criterion for Density Matrices, *Phys. Rev. Lett.* **77**, 1413 (1996).
- [30] T. Takayanagi and K. Umemoto, Entanglement of purification through holographic duality, *Nat. Phys.* **14**, 573 (2018).
- [31] P. Nguyen, T. Devakul, M.G. Halbasch, M.P. Zaletel, and B. Swingle, Entanglement of purification: From spin chains to holography, *J. High Energy Phys.* **01** (2018) 098.
- [32] J. Kudler-Flam and S. Ryu, Entanglement negativity and minimal entanglement wedge cross sections in holographic theories, *Phys. Rev. D* **99**, 106014 (2019).
- [33] Y. Kusuki, J. Kudler-Flam, and S. Ryu, Derivation of Holographic Negativity in AdS₃/CFT₂, *Phys. Rev. Lett.* **123**, 131603 (2019).
- [34] P. Chaturvedi, V. Malvimat, and G. Sengupta, Entanglement negativity, holography and black holes, *Eur. Phys. J. C* **78**, 499 (2018).
- [35] P. Chaturvedi, V. Malvimat, and G. Sengupta, Holographic quantum entanglement negativity, *J. High Energy Phys.* **05** (2018) 172.
- [36] P. Jain, V. Malvimat, S. Mondal, and G. Sengupta, Holographic entanglement negativity conjecture for adjacent intervals in AdS₃/CFT₂, *Phys. Lett. B* **793**, 104 (2019).
- [37] P. Jain, V. Malvimat, S. Mondal, and G. Sengupta, Holographic entanglement negativity for adjacent subsystems in AdS_{d+1}/CFT_d, *Eur. Phys. J. Plus* **133**, 300 (2018).
- [38] P. Jain, V. Malvimat, S. Mondal, and G. Sengupta, Covariant holographic entanglement negativity for adjacent subsystems in AdS₃/CFT₂, *Nucl. Phys.* **B945**, 114683 (2019).
- [39] P. Jain, V. Malvimat, S. Mondal, and G. Sengupta, Holographic entanglement negativity for conformal field theories with a conserved charge, *Eur. Phys. J. C* **78**, 908 (2018).
- [40] V. Malvimat, S. Mondal, B. Paul, and G. Sengupta, Holographic entanglement negativity for disjoint intervals in AdS₃/CFT₂, *Eur. Phys. J. C* **79**, 191 (2019).
- [41] V. Malvimat, H. Parihar, B. Paul, and G. Sengupta, Entanglement negativity in galilean conformal field theories, *Phys. Rev. D* **100**, 026001 (2019).
- [42] J. Kumar Basak, H. Parihar, B. Paul, and G. Sengupta, Holographic entanglement negativity for disjoint subsystems in AdS_{d+1}/CFT_d, [arXiv:2001.10534](https://arxiv.org/abs/2001.10534).
- [43] V. Malvimat, S. Mondal, and G. Sengupta, Time evolution of entanglement negativity from black hole interiors, *J. High Energy Phys.* **05** (2019) 183.
- [44] S. Dutta and T. Faulkner, A canonical purification for the entanglement wedge cross-section, *J. High Energy Phys.* **03** (2021) 178.
- [45] K. Tamaoka, Entanglement Wedge Cross Section from the Dual Density Matrix, *Phys. Rev. Lett.* **122**, 141601 (2019).
- [46] C. Akers and P. Rath, Entanglement wedge cross sections require tripartite entanglement, *J. High Energy Phys.* **04** (2020) 208.
- [47] P. Jain and S. Mahapatra, Mixed state entanglement measures as probe for confinement, *Phys. Rev. D* **102**, 126022 (2020).
- [48] P. Caputa, M. Miyaji, T. Takayanagi, and K. Umemoto, Holographic Entanglement of Purification from Conformal Field Theories, *Phys. Rev. Lett.* **122**, 111601 (2019).
- [49] K. Umemoto and Y. Zhou, Entanglement of purification for multipartite states and its holographic dual, *J. High Energy Phys.* **10** (2018) 152.

- [50] N. Bao and I. F. Halpern, Conditional and multipartite entanglements of purification and holography, *Phys. Rev. D* **99**, 046010 (2019).
- [51] R. Espíndola, A. Guijosa, and J. F. Pedraza, Entanglement wedge reconstruction and entanglement of purification, *Eur. Phys. J. C* **78**, 646 (2018).
- [52] H. S. Jeong, K. Y. Kim, and M. Nishida, Reflected entropy and entanglement wedge cross section with the first order correction, *J. High Energy Phys.* **12** (2019) 170.
- [53] N. Jokela and A. Pönni, Notes on entanglement wedge cross sections, *J. High Energy Phys.* **07** (2019) 087.
- [54] M. Ghodrati, Encoded information of mixed correlations: The views from one dimension higher, [arXiv:2209.04548](https://arxiv.org/abs/2209.04548).
- [55] A. Bhattacharyya, A. Jahn, T. Takayanagi, and K. Umemoto, Entanglement of Purification in Many Body Systems and Symmetry Breaking, *Phys. Rev. Lett.* **122**, 201601 (2019).
- [56] H. A. Camargo, L. Hackl, M. P. Heller, A. Jahn, and B. Windt, Long Distance Entanglement of Purification and Reflected Entropy in Conformal Field Theory, *Phys. Rev. Lett.* **127**, 141604 (2021).
- [57] M. C. Banuls, M. P. Heller, K. Jansen, J. Knaute, and V. Svensson, A quantum information perspective on meson melting, [arXiv:2206.10528](https://arxiv.org/abs/2206.10528).
- [58] M. Asadi, B. Amrahi, and H. Eshaghi-Kenari, Probing phase structure of strongly coupled matter with holographic entanglement measures, *Eur. Phys. J. C* **83**, 69 (2023).
- [59] M. Ali-Akbari, M. Asadi, and B. Amrahi, Non-conformal behavior of holographic entanglement measures, *J. High Energy Phys.* **04** (2022) 014.
- [60] M. J. Vasli, M. R. Mohammadi Mozaffar, K. Babaei Velni, and M. Sahraei, Holographic study of reflected entropy in anisotropic theories, *Phys. Rev. D* **107**, 026012 (2023).
- [61] P. Liu, C. Niu, Z. J. Shi, and C. Y. Zhang, Entanglement wedge minimum cross-section in holographic massive gravity theory, *J. High Energy Phys.* **08** (2021) 113.
- [62] P. Liu and J. P. Wu, Mixed state entanglement and thermal phase transitions, *Phys. Rev. D* **104**, 046017 (2021).
- [63] A. Saha and S. Gangopadhyay, Holographic study of entanglement and complexity for mixed states, *Phys. Rev. D* **103**, 086002 (2021).
- [64] A. R. Chowdhury, A. Saha, and S. Gangopadhyay, Entanglement wedge cross-section for noncommutative Yang-Mills theory, *J. High Energy Phys.* **02** (2022) 192.
- [65] J. Casalderrey-Solana, H. Liu, D. Mateos, K. Rajagopal, and U. A. Wiedemann, *Gauge/String Duality, Hot QCD and Heavy Ion Collisions* (Cambridge University Press, Cambridge, England, 2014), ISBN 978-1-139-13674-7.
- [66] S. S. Gubser and A. Karch, From gauge-string duality to strong interactions: A Pedestrian's Guide, *Annu. Rev. Nucl. Part. Sci.* **59**, 145 (2009).
- [67] M. Järvinen, Holographic modeling of nuclear matter and neutron stars, *Eur. Phys. J. C* **82**, 282 (2022).
- [68] U. Gursoy, E. Kiritsis, L. Mazzanti, G. Michalogiorgakis, and F. Nitti, Improved holographic QCD, *Lect. Notes Phys.* **828**, 79 (2011).
- [69] V. Skokov, A. Y. Illarionov, and V. Toneev, Estimate of the magnetic field strength in heavy-ion collisions, *Int. J. Mod. Phys. A* **24**, 5925 (2009).
- [70] A. Bzdak and V. Skokov, Event-by-event fluctuations of magnetic and electric fields in heavy ion collisions, *Phys. Lett. B* **710**, 171 (2012).
- [71] V. Voronyuk, V. D. Toneev, W. Cassing, E. L. Bratkovskaya, V. P. Konchakovski, and S. A. Voloshin, Electromagnetic field evolution in relativistic heavy-ion collisions, *Phys. Rev. C* **83**, 054911 (2011).
- [72] W. T. Deng and X. G. Huang, Event-by-event generation of electromagnetic fields in heavy-ion collisions, *Phys. Rev. C* **85**, 044907 (2012).
- [73] M. D'Elia, S. Mukherjee, and F. Sanfilippo, QCD phase transition in a strong magnetic background, *Phys. Rev. D* **82**, 051501 (2010).
- [74] M. D'Elia, L. Maio, F. Sanfilippo, and A. Stanzione, Confining and chiral properties of QCD in extremely strong magnetic fields, *Phys. Rev. D* **104**, 114512 (2021).
- [75] K. Tuchin, Particle production in strong electromagnetic fields in relativistic heavy-ion collisions, *Adv. High Energy Phys.* **2013**, 490495 (2013).
- [76] K. Tuchin, Time and space dependence of the electromagnetic field in relativistic heavy-ion collisions, *Phys. Rev. C* **88**, 024911 (2013).
- [77] L. McLerran and V. Skokov, Comments about the electromagnetic field in heavy-ion collisions, *Nucl. Phys. A* **929**, 184 (2014).
- [78] G. S. Bali, F. Bruckmann, G. Endrodi, Z. Fodor, S. D. Katz, S. Krieg, A. Schafer, and K. K. Szabo, The QCD phase diagram for external magnetic fields, *J. High Energy Phys.* **02** (2012) 044.
- [79] G. S. Bali, F. Bruckmann, G. Endrodi, Z. Fodor, S. D. Katz, and A. Schafer, QCD quark condensate in external magnetic fields, *Phys. Rev. D* **86**, 071502 (2012).
- [80] E. M. Ilgenfritz, M. Muller-Preussker, B. Petersson, and A. Schreiber, Magnetic catalysis (and inverse catalysis) at finite temperature in two-color lattice QCD, *Phys. Rev. D* **89**, 054512 (2014).
- [81] F. Bruckmann, G. Endrodi, and T. G. Kovacs, Inverse magnetic catalysis and the Polyakov loop, *J. High Energy Phys.* **04** (2013) 112.
- [82] K. Fukushima and Y. Hidaka, Magnetic Catalysis Versus Magnetic Inhibition, *Phys. Rev. Lett.* **110**, 031601 (2013).
- [83] M. Ferreira, P. Costa, O. Lourenço, T. Frederico, and C. Providência, Inverse magnetic catalysis in the (2 + 1)-flavor Nambu-Jona-Lasinio and Polyakov-Nambu-Jona-Lasinio models, *Phys. Rev. D* **89**, 116011 (2014).
- [84] N. Mueller and J. M. Pawłowski, Magnetic catalysis and inverse magnetic catalysis in QCD, *Phys. Rev. D* **91**, 116010 (2015).
- [85] G. S. Bali, F. Bruckmann, G. Endrodi, F. Gruber, and A. Schafer, Magnetic field-induced gluonic (inverse) catalysis and pressure (an)isotropy in QCD, *J. High Energy Phys.* **04** (2013) 130.
- [86] E. S. Fraga and L. F. Palhares, Deconfinement in the presence of a strong magnetic background: An exercise within the MIT bag model, *Phys. Rev. D* **86**, 016008 (2012).
- [87] A. Ayala, M. Loewe, A. J. Mizher, and R. Zamora, Inverse magnetic catalysis for the chiral transition induced by thermo-magnetic effects on the coupling constant, *Phys. Rev. D* **90**, 036001 (2014).

- [88] A. Ayala, M. Loewe, and R. Zamora, Inverse magnetic catalysis in the linear sigma model with quarks, *Phys. Rev. D* **91**, 016002 (2015).
- [89] E. S. Fraga, J. Noronha, and L. F. Palhares, Large N_c deconfinement transition in the presence of a magnetic field, *Phys. Rev. D* **87**, 114014 (2013).
- [90] C. Bonati, M. D’Elia, M. Mariti, M. Mesiti, F. Negro, and F. Sanfilippo, Anisotropy of the quark-antiquark potential in a magnetic field, *Phys. Rev. D* **89**, 114502 (2014).
- [91] C. Bonati, M. D’Elia, M. Mariti, M. Mesiti, F. Negro, A. Rucci, and F. Sanfilippo, Magnetic field effects on the static quark potential at zero and finite temperature, *Phys. Rev. D* **94**, 094007 (2016).
- [92] K. Fukushima, D. E. Kharzeev, and H. J. Warringa, The chiral magnetic effect, *Phys. Rev. D* **78**, 074033 (2008).
- [93] D. E. Kharzeev, L. D. McLerran, and H. J. Warringa, The effects of topological charge change in heavy ion collisions: ‘Event by event P and CP violation’, *Nucl. Phys. A* **803**, 227 (2008).
- [94] D. E. Kharzeev, J. Liao, S. A. Voloshin, and G. Wang, Chiral magnetic and vortical effects in high-energy nuclear collisions—A status report, *Prog. Part. Nucl. Phys.* **88**, 1 (2016).
- [95] C. V. Johnson and A. Kundu, External fields and chiral symmetry breaking in the Sakai-Sugimoto model, *J. High Energy Phys.* **12** (2008) 053.
- [96] N. Callebaut, D. Dudal, and H. Verschelde, Holographic ρ mesons in an external magnetic field, *J. High Energy Phys.* **03** (2013) 033.
- [97] N. Callebaut and D. Dudal, Transition temperature(s) of magnetized two-flavor holographic QCD, *Phys. Rev. D* **87**, 106002 (2013).
- [98] D. Dudal, D. R. Granado, and T. G. Mertens, No inverse magnetic catalysis in the QCD hard and soft wall models, *Phys. Rev. D* **93**, 125004 (2016).
- [99] D. Dudal and T. G. Mertens, Melting of charmonium in a magnetic field from an effective AdS/QCD model, *Phys. Rev. D* **91**, 086002 (2015).
- [100] D. Dudal and T. G. Mertens, Holographic estimate of heavy quark diffusion in a magnetic field, *Phys. Rev. D* **97**, 054035 (2018).
- [101] U. Gürsoy, M. Jarvinen, and G. Nijs, Holographic QCD in the Veneziano Limit at a Finite Magnetic Field and Chemical Potential, *Phys. Rev. Lett.* **120**, 242002 (2018).
- [102] N. Jokela, A. V. Ramallo, and D. Zoakos, Magnetic catalysis in flavored ABJM, *J. High Energy Phys.* **02** (2014) 021.
- [103] U. Gürsoy, I. Iatrakis, M. Järvinen, and G. Nijs, Inverse magnetic catalysis from improved holographic QCD in the veneziano limit, *J. High Energy Phys.* **03** (2017) 053.
- [104] D. Li, M. Huang, Y. Yang, and P. H. Yuan, Inverse magnetic catalysis in the soft-wall model of AdS/QCD, *J. High Energy Phys.* **02** (2017) 030.
- [105] R. Critelli, R. Rougemont, S. I. Finazzo, and J. Noronha, Polyakov loop and heavy quark entropy in strong magnetic fields from holographic black hole engineering, *Phys. Rev. D* **94**, 125019 (2016).
- [106] D. Giataganas, U. Gürsoy, and J. F. Pedraza, Strongly-Coupled Anisotropic Gauge Theories and Holography, *Phys. Rev. Lett.* **121**, 121601 (2018).
- [107] U. Gürsoy, M. Järvinen, G. Nijs, and J. F. Pedraza, On the interplay between magnetic field and anisotropy in holographic QCD, *J. High Energy Phys.* **03** (2021) 180.
- [108] U. Gürsoy, M. Järvinen, G. Nijs, and J. F. Pedraza, Inverse anisotropic catalysis in holographic QCD, *J. High Energy Phys.* **04** (2019) 071; **09** (2020) 059(E).
- [109] D. M. Rodrigues, E. Folco Capossoli, and H. Boschi-Filho, Deconfinement phase transition in a magnetic field in $2 + 1$ dimensions from holographic models, *Phys. Lett. B* **780**, 37 (2018).
- [110] D. M. Rodrigues, D. Li, E. Folco Capossoli, and H. Boschi-Filho, Chiral symmetry breaking and restoration in $2 + 1$ dimensions from holography: Magnetic and inverse magnetic catalysis, *Phys. Rev. D* **98**, 106007 (2018).
- [111] H. Bohra, D. Dudal, A. Hajilou, and S. Mahapatra, Anisotropic string tensions and inversely magnetic catalyzed deconfinement from a dynamical AdS/QCD model, *Phys. Lett. B* **801**, 135184 (2020).
- [112] H. Bohra, D. Dudal, A. Hajilou, and S. Mahapatra, Chiral transition in the probe approximation from an Einstein-Maxwell-dilaton gravity model, *Phys. Rev. D* **103**, 086021 (2021).
- [113] D. Dudal, A. Hajilou, and S. Mahapatra, A quenched 2-flavour Einstein-Maxwell-dilaton gauge-gravity model, *Eur. Phys. J. A* **57**, 142 (2021).
- [114] I. Y. Aref’eva, A. Ermakov, K. Rannu, and P. Slepov, Holographic model for light quarks in anisotropic hot dense QGP with external magnetic field, *Eur. Phys. J. C* **83**, 79 (2023).
- [115] I. Y. Aref’eva, K. Rannu, and P. Slepov, Holographic model for heavy quarks in anisotropic hot dense QGP with external magnetic field, *J. High Energy Phys.* **07** (2021) 161.
- [116] I. Aref’eva, K. Rannu, and P. Slepov, Orientation dependence of confinement-deconfinement phase transition in anisotropic media, *Phys. Lett. B* **792**, 470 (2019).
- [117] I. Aref’eva and K. Rannu, Holographic anisotropic background with confinement-deconfinement phase transition, *J. High Energy Phys.* **05** (2018) 206.
- [118] S. S. Jena, B. Shukla, D. Dudal, and S. Mahapatra, Entropic force and real-time dynamics of holographic quarkonium in a magnetic field, *Phys. Rev. D* **105**, 086011 (2022).
- [119] A. Ballon-Bayona, J. P. Shock, and D. Zoakos, Magnetising the $\mathcal{N} = 4$ super Yang-Mills plasma, *J. High Energy Phys.* **06** (2022) 154.
- [120] I. Y. Aref’eva, K. Rannu, and P. Slepov, Energy loss in holographic anisotropic model for heavy quarks in external magnetic field, [arXiv:2012.05758](https://arxiv.org/abs/2012.05758).
- [121] A. Ballon-Bayona, J. P. Shock, and D. Zoakos, Magnetic catalysis and the chiral condensate in holographic QCD, *J. High Energy Phys.* **10** (2020) 193.
- [122] S. He, Y. Yang, and P. H. Yuan, Analytic study of magnetic catalysis in holographic QCD, [arXiv:2004.01965](https://arxiv.org/abs/2004.01965).
- [123] Z. R. Zhu, D. f. Hou, and X. Chen, Potential analysis of holographic Schwinger effect in the magnetized background, *Eur. Phys. J. C* **80**, 550 (2020).
- [124] N. R. F. Braga and R. da Mata, Configuration entropy description of charmonium dissociation under the influence of magnetic fields, *Phys. Lett. B* **811**, 135918 (2020).

- [125] K. A. Mamo, Inverse magnetic catalysis in holographic models of QCD, *J. High Energy Phys.* **05** (2015) 121.
- [126] D. Ávila, V. Jahnke, and L. Patiño, Chaos, diffusivity, and spreading of entanglement in magnetic branes, and the strengthening of the internal interaction, *J. High Energy Phys.* **09** (2018) 131.
- [127] D. Giataganas, Probing strongly coupled anisotropic plasma, *J. High Energy Phys.* **07** (2012) 031.
- [128] M. Abdallah *et al.* (STAR Collaboration), Search for the chiral magnetic effect with isobar collisions at $\sqrt{s_{NN}} = 200$ GeV by the STAR Collaboration at the BNL Relativistic Heavy Ion Collider, *Phys. Rev. C* **105**, 014901 (2022).
- [129] R. C. Duncan and C. Thompson, Formation of very strongly magnetized neutron stars—implications for gamma-ray bursts, *Astrophys. J. Lett.* **392**, L9 (1992).
- [130] D. Grasso and H. R. Rubinstein, Magnetic fields in the early universe, *Phys. Rep.* **348**, 163 (2001).
- [131] C. Ecker, M. Järvinen, G. Nijs, and W. van der Schee, Gravitational waves from holographic neutron star mergers, *Phys. Rev. D* **101**, 103006 (2020).
- [132] D. E. Kharzeev, K. Landsteiner, A. Schmitt, and H. U. Yee, ‘Strongly interacting matter in magnetic fields’: An overview, *Lect. Notes Phys.* **871**, 1 (2013).
- [133] V. A. Miransky and I. A. Shovkovy, Quantum field theory in a magnetic field: From quantum chromodynamics to graphene and Dirac semimetals, *Phys. Rep.* **576**, 1 (2015).
- [134] P. V. Buividovich and M. I. Polikarpov, Numerical study of entanglement entropy in SU(2) lattice gauge theory, *Nucl. Phys.* **B802**, 458 (2008).
- [135] P. V. Buividovich and M. I. Polikarpov, Entanglement entropy in gauge theories and the holographic principle for electric strings, *Phys. Lett. B* **670**, 141 (2008).
- [136] E. Itou, K. Nagata, Y. Nakagawa, A. Nakamura, and V. I. Zakharov, Entanglement in four-dimensional SU(3) gauge theory, *Prog. Theor. Exp. Phys.* **2016**, 061B01 (2016).
- [137] A. Rabenstein, N. Bodendorfer, P. Buividovich, and A. Schäfer, Lattice study of Rényi entanglement entropy in $SU(N_c)$ lattice Yang-Mills theory with $N_c = 2, 3, 4$, *Phys. Rev. D* **100**, 034504 (2019).
- [138] D. Dudal and S. Mahapatra, Confining gauge theories and holographic entanglement entropy with a magnetic field, *J. High Energy Phys.* **04** (2017) 031.
- [139] D. Dudal and S. Mahapatra, Interplay between the holographic QCD phase diagram and entanglement entropy, *J. High Energy Phys.* **07** (2018) 120.
- [140] S. Mahapatra, Interplay between the holographic QCD phase diagram and mutual & n -partite information, *J. High Energy Phys.* **04** (2019) 137.
- [141] U. Kol, C. Nunez, D. Schofield, J. Sonnenschein, and M. Warschawski, Confinement, phase transitions and non-locality in the entanglement entropy, *J. High Energy Phys.* **06** (2014) 005.
- [142] O. Ben-Ami, D. Carmi, and J. Sonnenschein, Holographic entanglement entropy of multiple strips, *J. High Energy Phys.* **11** (2014) 144.
- [143] M. Fujita, T. Nishioka, and T. Takayanagi, Geometric entropy and hagedorn/deconfinement transition, *J. High Energy Phys.* **09** (2008) 016.
- [144] A. Lewkowycz, Holographic entanglement entropy and confinement, *J. High Energy Phys.* **05** (2012) 032.
- [145] G. Georgiou and D. Zoakos, Entanglement entropy of the Klebanov-Strassler model with dynamical flavors, *J. High Energy Phys.* **07** (2015) 003.
- [146] N. Kim, Holographic entanglement entropy of confining gauge theories with flavor, *Phys. Lett. B* **720**, 232 (2013).
- [147] M. Ghodrati, Schwinger effect and entanglement entropy in confining geometries, *Phys. Rev. D* **92**, 065015 (2015).
- [148] M. Ali-Akbari and M. Lezgi, Holographic QCD, entanglement entropy, and critical temperature, *Phys. Rev. D* **96**, 086014 (2017).
- [149] J. Knaute and B. Kämpfer, Holographic entanglement entropy in the QCD phase diagram with a critical point, *Phys. Rev. D* **96**, 106003 (2017).
- [150] M. M. Anber and B. J. Kolligs, Entanglement entropy, dualities, and deconfinement in gauge theories, *J. High Energy Phys.* **08** (2018) 175.
- [151] I. Y. Aref’eva, A. Patrushev, and P. Slepov, Holographic entanglement entropy in anisotropic background with confinement-deconfinement phase transition, *J. High Energy Phys.* **07** (2020) 043.
- [152] P. Slepov, Entanglement entropy in strongly correlated systems with confinement/deconfinement phase transition and anisotropy, *EPJ Web Conf.* **222**, 03024 (2019).
- [153] P. Liu, C. Niu, and J. P. Wu, The effect of anisotropy on holographic entanglement entropy and mutual information, *Phys. Lett. B* **796**, 155 (2019).
- [154] M. Fujita, S. He, and Y. Sun, Thermodynamical property of entanglement entropy and deconfinement phase transition, *Phys. Rev. D* **102**, 126019 (2020).
- [155] G. Fu, P. Liu, H. Gong, X. M. Kuang, and J. P. Wu, Holographic informational properties for a specific Einstein-Maxwell-dilaton gravity theory, *Phys. Rev. D* **104**, 026016 (2021).
- [156] N. Jokela and J. G. Subils, Is entanglement a probe of confinement?, *J. High Energy Phys.* **02** (2021) 147.
- [157] B. S. DiNunno, N. Jokela, J. F. Pedraza, and A. Pönni, Quantum information probes of charge fractionalization in large- N gauge theories, *J. High Energy Phys.* **05** (2021) 149.
- [158] M. Ghodrati, Correlations of mixed systems in confining backgrounds, *Eur. Phys. J. C* **82**, 531 (2022).
- [159] G. Yadav, V. Yadav, and A. Misra, \mathcal{M} CTEQ (\mathcal{M} chiral perturbation theory-compatible deconfinement temperature and entanglement entropy up to terms Quartic in curvature) and FM (flavor memory), *J. High Energy Phys.* **10** (2021) 220.
- [160] C. S. Chu and D. Giataganas, c -theorem for anisotropic RG flows from holographic entanglement entropy, *Phys. Rev. D* **101**, 046007 (2020).
- [161] C. Cartwright and M. Kaminski, Inverted c -functions in thermal states, *J. High Energy Phys.* **01** (2022) 161.
- [162] M. Fromm, J. Langelage, S. Lottini, and O. Philipsen, The QCD deconfinement transition for heavy quarks and all baryon chemical potentials, *J. High Energy Phys.* **01** (2012) 042.
- [163] D. Dudal and S. Mahapatra, Thermal entropy of a quark-antiquark pair above and below deconfinement from a dynamical holographic QCD model, *Phys. Rev. D* **96**, 126010 (2017).

- [164] P. Breitenlohner and D. Z. Freedman, Positive energy in anti-de Sitter backgrounds and gauged extended supergravity, *Phys. Lett.* **115B**, 197 (1982).
- [165] S. S. Gubser, Curvature singularities: The good, the bad, and the naked, *Adv. Theor. Math. Phys.* **4**, 679 (2000).
- [166] P. Calabrese and J. Cardy, Entanglement entropy and conformal field theory, *J. Phys. A* **42**, 504005 (2009).
- [167] P. Hayden, M. Headrick, and A. Maloney, Holographic mutual information is monogamous, *Phys. Rev. D* **87**, 046003 (2013).
- [168] M. Headrick, Entanglement Renyi entropies in holographic theories, *Phys. Rev. D* **82**, 126010 (2010).
- [169] W. Fischler, A. Kundu, and S. Kundu, Holographic mutual information at finite temperature, *Phys. Rev. D* **87**, 126012 (2013).
- [170] S. Kundu and J. F. Pedraza, Aspects of holographic entanglement at finite temperature and chemical potential, *J. High Energy Phys.* **08** (2016) 177.
- [171] H. Casini, M. Huerta, R. C. Myers, and A. Yale, Mutual information and the F-theorem, *J. High Energy Phys.* **10** (2015) 003.
- [172] V. Balasubramanian, N. Jokela, A. Pönni, and A. V. Ramallo, Information flows in strongly coupled ABJM theory, *J. High Energy Phys.* **01** (2019) 232.
- [173] J. Cardy, Some results on the mutual information of disjoint regions in higher dimensions, *J. Phys. A* **46**, 285402 (2013).
- [174] A. J. Larkoski, J. Thaler, and W. J. Waalewijn, Gaining (mutual) information about quark/gluon discrimination, *J. High Energy Phys.* **11** (2014) 129.
- [175] C. A. Agón, P. Bueno, O. Lasso Andino, and A. Vilar López, Aspects of N-partite information in conformal field theories, [arXiv:2209.14311](https://arxiv.org/abs/2209.14311).
- [176] P. Calabrese, J. Cardy, and E. Tonni, Entanglement Negativity in Quantum Field Theory, *Phys. Rev. Lett.* **109**, 130502 (2012).
- [177] P. Calabrese, J. Cardy, and E. Tonni, Entanglement negativity in extended systems: A field theoretical approach, *J. Stat. Mech.* (2013) P02008.
- [178] V. Alba, Entanglement negativity and conformal field theory: A Monte Carlo study, *J. Stat. Mech.* (2013) P05013.
- [179] P. Calabrese, L. Tagliacozzo, and E. Tonni, Entanglement negativity in the critical Ising chain, *J. Stat. Mech.* (2013) P05002.
- [180] P. Ruggiero, V. Alba, and P. Calabrese, Entanglement negativity in random spin chains, *Phys. Rev. B* **94**, 035152 (2016).
- [181] M. Hoogeveen and B. Doyon, Entanglement negativity and entropy in non-equilibrium conformal field theory, *Nucl. Phys.* **B898**, 78 (2015).
- [182] O. Blondeau-Fournier, O. A. Castro-Alvaredo, and B. Doyon, Universal scaling of the logarithmic negativity in massive quantum field theory, *J. Phys. A* **49**, 125401 (2016).
- [183] C. Castelnovo, Negativity and topological order in the toric code, *Phys. Rev. A* **88**, 042319 (2013).
- [184] Y. A. Lee and G. Vidal, Entanglement negativity and topological order, *Phys. Rev. A* **88**, 042318 (2013).
- [185] V. Eisler and Z. Zimborás, Entanglement negativity in two-dimensional free lattice models, *Phys. Rev. B* **93**, 115148 (2016).
- [186] X. Wen, P. Y. Chang, and S. Ryu, Entanglement negativity after a local quantum quench in conformal field theories, *Phys. Rev. B* **92**, 075109 (2015).
- [187] X. Wen, P. Y. Chang, and S. Ryu, Topological entanglement negativity in Chern-Simons theories, *J. High Energy Phys.* **09** (2016) 012.
- [188] M. Rangamani and M. Rota, Comments on entanglement negativity in holographic field theories, *J. High Energy Phys.* **10** (2014) 060.